



HAL
open science

A micromechanical analysis of swelling-induced embrittlement in neutron-irradiated austenitic stainless steels

Jeremy Hure, Arnaud Courcelle, Isabelle Turque

► **To cite this version:**

Jeremy Hure, Arnaud Courcelle, Isabelle Turque. A micromechanical analysis of swelling-induced embrittlement in neutron-irradiated austenitic stainless steels. *Journal of Nuclear Materials*, 2022, pp.153732. 10.1016/j.jnucmat.2022.153732 . cea-03748669

HAL Id: cea-03748669

<https://cea.hal.science/cea-03748669>

Submitted on 9 Aug 2022

HAL is a multi-disciplinary open access archive for the deposit and dissemination of scientific research documents, whether they are published or not. The documents may come from teaching and research institutions in France or abroad, or from public or private research centers.

L'archive ouverte pluridisciplinaire **HAL**, est destinée au dépôt et à la diffusion de documents scientifiques de niveau recherche, publiés ou non, émanant des établissements d'enseignement et de recherche français ou étrangers, des laboratoires publics ou privés.

A micromechanical analysis of swelling-induced embrittlement in neutron-irradiated austenitic stainless steels

J. Hure^{a,1}, A. Courcelle^a, I. Turque^a

^aUniversité Paris-Saclay, CEA, Service d'Étude des Matériaux Irradiés, 91191, Gif-sur-Yvette, France

Abstract

Swelling is commonly observed in austenitic stainless steels irradiated at high doses and high temperatures, such as fuel claddings in Fast-Breeder Reactors (FBR), as a consequence of the formation of irradiation-induced nanovoids. Macroscopic embrittlement has been reported above a critical swelling level. Several physical explanations have been proposed such as void-related fracture mechanisms and phase transformation associated with local changes of micro-chemistry. In addition, structural effects can affect the critical swelling level, tentatively explained by local corrosion, swelling gradient and bending effects. In order to address these phenomena, an extended experimental database is first presented, based on fuel pins irradiated in the Phénix fast reactor, showing the evolution of conventional tensile properties with swelling. In the present database, 15-15Ti specimens were irradiated from 30 to 120 dpa, with irradiation temperatures ranging from 400°C to 625°C and a maximum swelling of 11%. Other data published in scientific literature were also included in the analysis to extend the swelling range up to 30%. SEM and TEM analysis are also summarized to highlight specific embrittlement mechanisms related to the presence of voids. Theoretical analysis and finite element simulations are then performed based on porous materials constitutive equations in order to rationalize the experimental observations. Analytical and numerical results show that swelling-induced embrittlement can be understood from a mechanical perspective as a transition from void growth to void coalescence deformation mode. The effect of the spatial heterogeneity of void distribution is quantified and shown to be a key parameter. Structural effects coming from tests performed on ring and axial tensile specimens and from the presence of a swelling gradient in cladding thickness are also quantified. Numerical results are compared to experimental data, and a good agreement is observed.

Keywords:

Irradiation, Swelling, Austenitic steels, Embrittlement, Tensile test, Porous materials

1. Introduction

Neutron irradiation of metallic materials leads to the formation of crystallographic defects [1]. These microstructural evolutions are strongly dependent on both materials and irradiation conditions such as neutron spectrum, flux, fluence and temperature [2]. In the context of austenitic stainless steels used as fuel claddings in Fast Breeder Reactors (FBR), Cawthorne & Fulton [3] observed for the first time that nanometric voids can be formed under irradiation at high temperature and high fluence. The macroscopic counterpart of the presence of nanovoids in materials is a change of dimensions, referred to as void swelling [4]. From a structural point of view, void swelling can lead to severe distortions of fuel elements [5], compromising reactor coolant flows. After an incubation period of few tens of dpa, a swelling steady state as high as 1% per dpa can be reached for austenitic stainless steels [6]. Void swelling is highly dependent on the irradiation temperature, and also on the chemical composition of the material [6]. This dependence has been studied extensively in order to obtain swelling-resistant austenitic stainless steels for FBR fuel claddings, leading to optimized grades, or to the proposition of alternative materials [7]. Irradiation-induced voids are also observed in Light Water Reactors (LWR) internals structures [1] to a lesser extent due to the lower temperature. The reader is referred to [8] for details about void swelling and more generally about austenitic stainless steels used in nuclear applications.

Apart from dimensional stability, void swelling has been also related to embrittlement. Macroscopic ductility as well as fracture toughness of austenitic stainless steels decrease with irradiation irrespective of the irradiation temperature. This is the result of the hardening and loss of strain hardening capability induced by the presence of irradiation defects and dislocation network modifications [9, 10]. In most cases, the irradiated material remains ductile, and fracture is associated at the macroscopic scale with a measurable amount of plasticity. However, brittle-like behavior has been observed for irradiation conditions leading to large swelling [11]. Brittle failure of pressurized capsules made of 316 stainless steels irradiated at high fluences has been found in [12] for very low applied stress. Additional experimental observations have been added over the years. In [13], the observations of fracture surfaces showing facets-like features covered with dimples indicate that void-driven ductile fracture occurred parallel to grain boundaries. This scenario has been corroborated by Transmission Electron Microscope (TEM) observations showing larger voids close to grain boundaries. Evolutions of conventional tensile properties with swelling have been documented in [14, 15], showing a decrease of Ultimate Tensile Strength (UTS) with swelling. Moreover, a critical swelling level is observed above which no (plastic) elongation is

*Corresponding author: jeremy.hure@cea.fr

localization. Simulations performed in [33] account for random distribution of voids at the relevant (crystal) scale, but void coalescence is not studied. Finally, none of the previous studies have performed simulations on tensile specimens in order to assess structural effects.

Therefore, the objectives of the paper are twofold. The first is to provide an experimental database complementing the results shown in [8] regarding the evolution of conventional tensile properties with swelling and the occurrence of quasi-brittle behaviour. The second objective is to use homogenized porous models to simulate the experimental tests in order to highlight the key parameters controlling the embrittlement at both material and structural scales. The paper is organized as follows: in Section 2, the experimental database - materials, irradiation conditions, mechanical tests, observations - is presented. Modelling and numerical simulations are detailed in Section 3. Numerical results are described in Section 4, and key parameters are finally discussed in Section 5.

2. Experimental database

The experimental database is based on post-irradiation experiments (PIE) performed on fuel pins irradiated in the Phénix fast reactor located in France. During Phénix operation from 1973 up to decommission in 2010, numerous alloys in standard and experimental assemblies were tested in support of the R&D program on FBR [34]. First batches of fuel claddings were made of commercial annealed 316-type steel in the 70's and were gradually replaced by optimized cold-worked grades to achieve a better resistance to irradiation swelling and preserve good thermal creep properties at high temperature. Careful specifications of major (Ni, Cr) and minor (mainly Ti, C, Si, Mo, Mn and P) elements contents and optimization of fabrication process (thermal treatment and cold-work level) led to a family of swelling-resistant alloys called in the present paper 15-15Ti. In France, the latest generation of 15-15Ti named AIM1 (Austenitic Improved Material #1) can reach about 100 dpa with a moderate swelling and an acceptable degradation of mechanical properties [35]. Specification of AIM1 is close to other austenitic alloys studied in the international community such as DIN 1.4970 in Germany, optimized D9 in the US, AFIC1 in India, CHS-68 in Russia etc. In the present database, only cold-worked 15-15Ti fuel claddings were selected (cold-work levels from 20 to 25%). 15-15Ti alloys irradiated in Phénix over the years present slight variations of chemical composition within the range of values presented in Table 1. Before irradiation, external diameter of the claddings was specified to 6.55 mm and the initial thickness was 0.45 mm.

Table 1

Ranges of chemical composition in weight percent of cold-worked 15-15Ti irradiated in Phénix. Other trace elements are also present in the alloys but specified at a low level

Element	Cr	Ni	Mo	Mn	Si	C	Ti	P
wt% range	14-16	14-16	1.3-1.7	1.3-1.7	0.4- 0.9	0.08-0.12	0.3-0.5	< 0.04

2.1. Swelling and tensile properties

Prior to examinations, fuel pins from Phénix assemblies were defueled in hot laboratory (with both mechanical and chemical process) and cut into several samples. Cladding irradiation temperatures were estimated by neutronics and thermal computations. Irradiation temperatures range from 400 to 625°C. Fuel-pin cladding were irradiated up to 120 dpa with an helium generation rate of roughly 0.5 appm/dpa¹. During reactor operation, the irradiation temperature was not strictly constant and slightly decreased during reactor cycle. Irradiation temperatures quoted in the paper were averaged out over the assembly lifetime. In addition, a temperature gradient across cladding thickness was also present during irradiation. Thermal computations gave an estimate of around 50°C between the internal and the external part of the cladding. This temperature gradient may generate a significant swelling gradient in the thickness of the cladding. This point is discussed later on in the paper. Average swelling values were deduced from density measurements by immersion technique with an accuracy of about ±0.15%. This technique was considered more reliable than the one using TEM images of cavities.

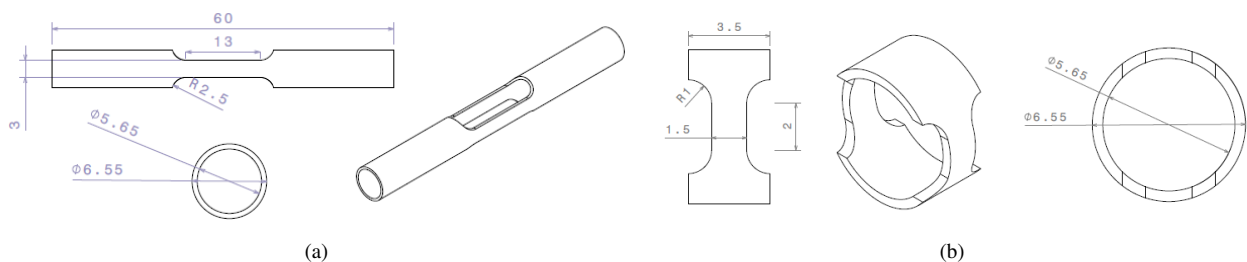


Fig. 2. Axial (a) and ring shape (b) tensile specimens machined in fuel pins to assess the mechanical properties as a function of irradiation conditions (Dimensions in mm)

¹It should be noted that the helium production affects swelling. However, this study deals only with the mechanical properties of a material containing nanovoids, and not with the mechanisms responsible for the formation of these voids.

Spark-erosion machining of axial and ring specimens was carried out at several pin heights to span irradiation temperatures from 400 to 625°C. Axial and circumferential tensile specimens are shown in Fig. 2. The gage length of the ring specimens is 2mm and the gage width is 1.5 mm (the diameter is 6.55 mm and the shoulders width is 3.5 mm). For the axial specimen, the gage length is 13 mm and the gage width is 3 mm (the diameter is 6.55 mm and the total height is 60 mm). The geometries of these specimens, similar to the ones used and assessed in [36], have been designed to comply with cladding geometry and hot cells testing constraints. Numerical finite-element simulations using isotropic plasticity for typical values encountered in the following confirmed that both geometries allow recovering yield stress and ultimate tensile strength values with a maximal error of 5%. Hot-cells tensile tests were conducted in air, at both 20°C and at the irradiation temperatures, with strain rates ranging from $3 \cdot 10^{-4} \text{s}^{-1}$ to $4.5 \cdot 10^{-4} \text{s}^{-1}$. Test temperature was monitored using thermocouples in contact with the specimens, with an accuracy of $\pm 1^\circ\text{C}$. Conventional tensile properties, yield stress YS (with an offset of 0.2%), ultimate tensile stress UTS, uniform plastic elongation UE and total plastic elongation TE were evaluated from the tensile curves (Fig. 1). Strictly speaking, the curves and the conventional tensile properties obtained on axial and ring specimens are not true tensile curves and conventional tensile properties due to the use of unstandardized samples. However, geometrical effects are known to be weak for axial specimens, and ring specimens lead to results consistent to axial specimens for YS, UTS and TE (Appendix A). All data correspond to relatively high irradiation levels ($> 30 \text{ dpa}$), *i.e.*, higher than the saturation value for many irradiation-induced crystallographic defects (nanoprecipitates, Frank loop, dislocation) *except* nanovoids. Thus, for a given swelling level, the dose dependence of tensile properties is expected to be small above 30 dpa. In the following, tensile properties are thus evaluated as a function of swelling. Furthermore, the relatively narrow range of irradiation temperature T in the range $[430 - 560]^\circ\text{C}$ supports the hypothesis made in the following that only temperature and swelling affect the conventional tensile properties reported hereafter. For completeness, it should however be noted that differences of irradiation-induced precipitates might exist. The potential effect of the presence of precipitates is discussed in the last section as a perspective.

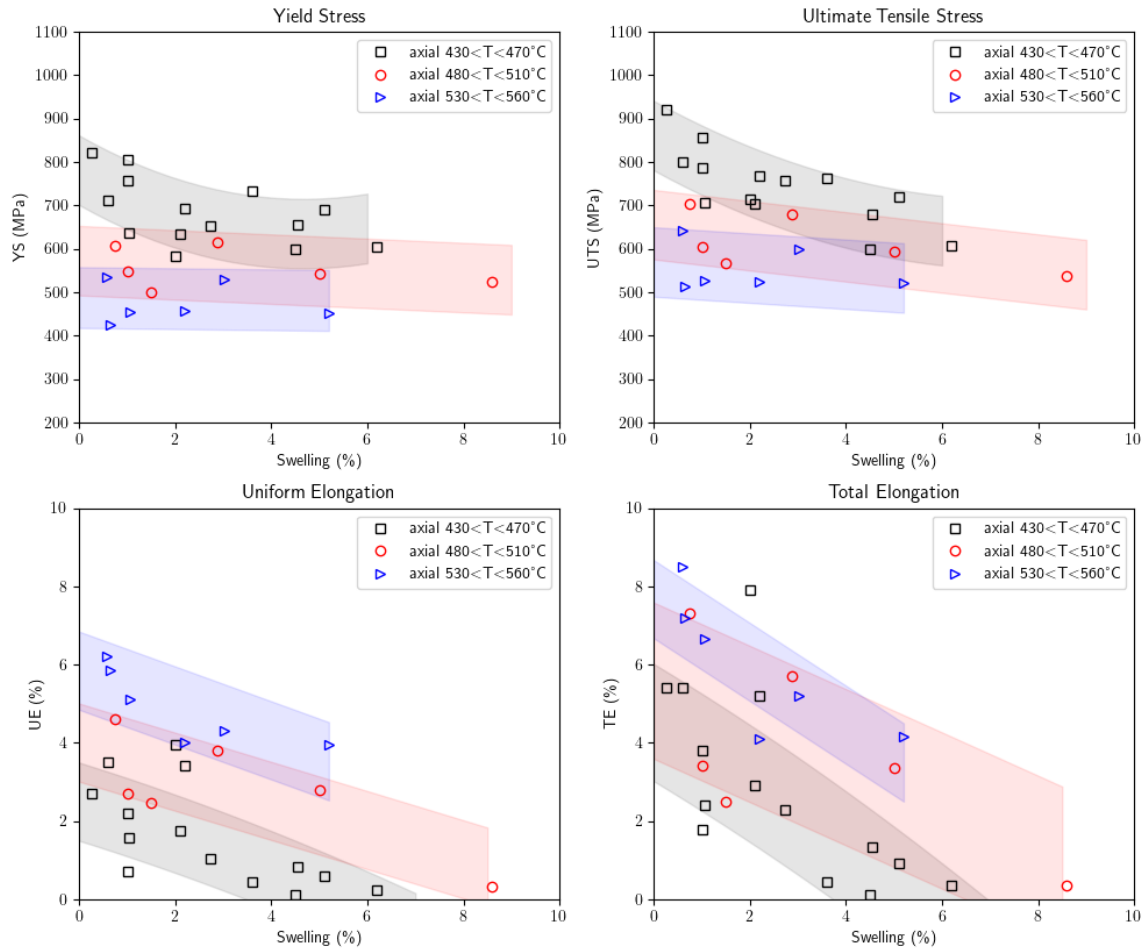


Fig. 3. Synthesis of conventional tensile properties measured with axial specimens for three different irradiation temperature ranges ($430 < T < 470^\circ\text{C}$, $480 < T < 510^\circ\text{C}$, $530 < T < 560^\circ\text{C}$) as a function of swelling. Test temperature is equal to the average irradiation temperature.

Results for axial specimens (Fig. 2(a)) are first shown in Fig. 3 as a function of swelling for three temperature ranges. Up to 6-8% the effect of swelling is rather small on yield stress and ultimate tensile stress whatever the temperature range, with an overall slight decrease. Moreover, the higher the test temperature, the lower the stresses, consistently with the effect of temperature on mechanical properties. In contrast, uniform and total elongations decrease drastically as a function of swelling, down to negligible values above 6% swelling for irradiation temperatures below 500°C, *i.e.*, quasi-embrittlement occurs. The evolutions of conventional tensile properties as a function of swelling are in qualitative agreement with the data reported in [14, 15]. In the latter, higher swelling levels are available, allowing to observe the

strong decrease of yield and ultimate tensile stress in the brittle regime. As shown in Figure 4 ring tensile tests exhibit similar trends but show a higher dispersion in experimental data. The main difference between tensile properties measured by ring and axial specimens concerns UE between 450 and 550°C, which is significantly lower in ring tensile tests. This structural effect is also observed restricting to data where swelling is negligible (<1%), as shown in Appendix A. Some ring tensile test data with brittle behavior were not included in the database because they showed signs of fuel-cladding chemical interaction (FCCI) responsible for early intergranular attack and grain-boundary embrittlement.

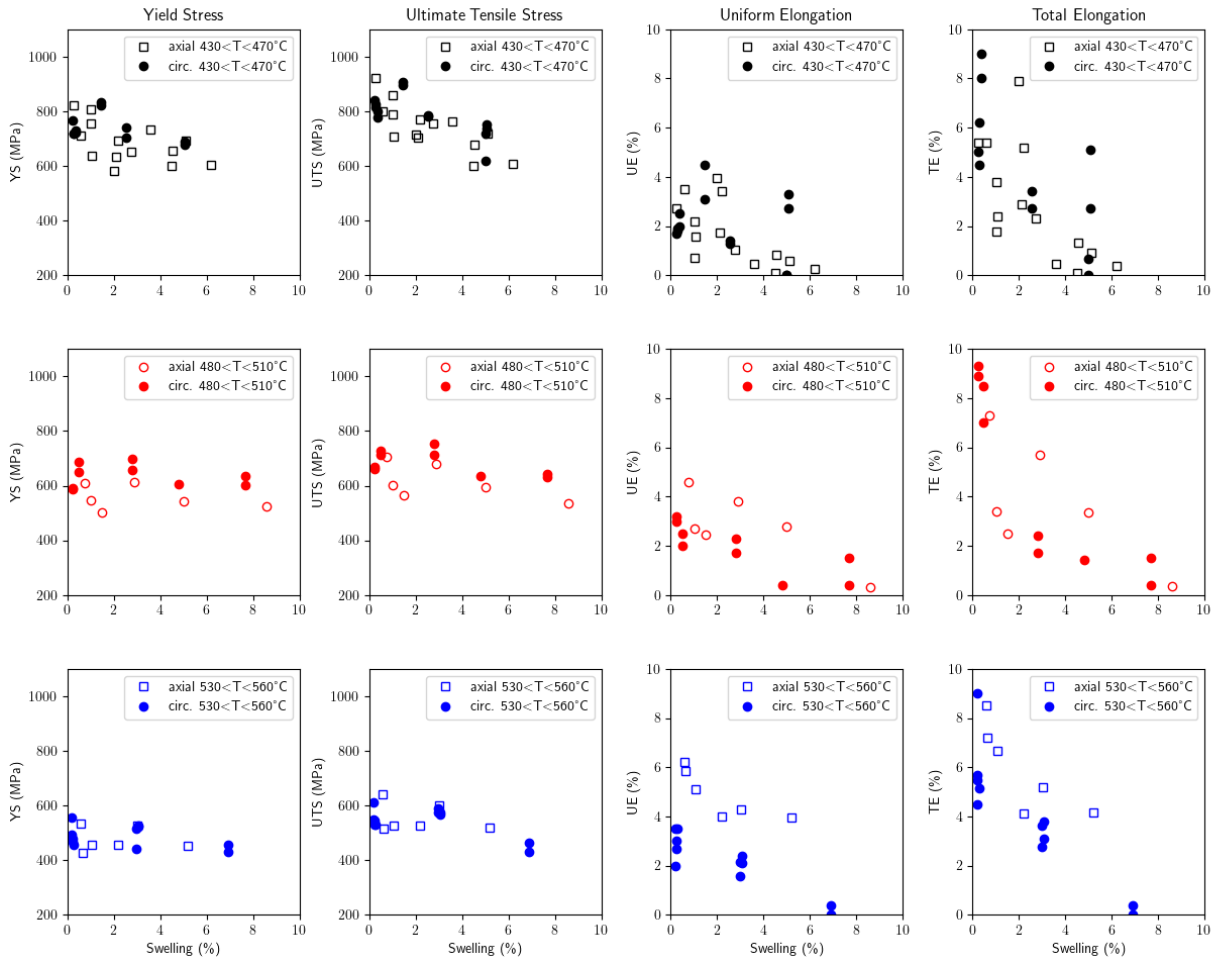


Fig. 4. Comparison of axial and ring conventional tensile properties for three different irradiation temperature ranges (430<T<470°C, 480<T<510°C, 530<T<560°C), as a function of swelling. Test temperature is equal to the average irradiation temperature.

In order to separate the effects of (irradiation and test) temperature T and swelling level S on the evolution of tensile properties and to assess the existence of master curves, a multiplicative decomposition of the effect of these variables is postulated. Conventional tensile properties X are expressed as $X(T, S) = X_T(T)X_S(S)$. The first term $X_T(T)$ is evaluated by using low-swelling values ($X_T(T) = X(T, S \approx 0)$) computed from the data shown in Appendix A, leading to Fig. 5. Although scatter coming from the initial data (Fig. 4) still appears after normalization, Fig. 5 enables gathering all data obtained at different temperatures on single curves, allowing to assess the effect of swelling independently of temperature. The effect of test geometry appears weak, except for yield stress where some outliers may require dedicated assessment. For all tensile properties, and for the range of swelling levels available in the database, clear decreasing trends are obtained, that can be described by linear evolutions (Eq. 2 and Table 2) independent of test geometry.

Table 2
Fitted slope of normalized tensile properties versus swelling (Eq. 2)

$$\frac{X(T, S)}{X(T, S \approx 0)} = \bar{X} \quad (1)$$

$$= 1 - \alpha_X S(\%) \quad (2)$$

Properties	α_X
YS	0.022
UTS	0.020
UE	0.103
TE	0.132

The evolution of the total elongation as a function of swelling indicates a quasi-embrittlement for $1 - \alpha_X S = 0 \Rightarrow S \approx 7.5\%$, providing an additional justification of the 6% embrittlement limit chosen in France as a design criteria for FBR. These results are in qualitative agreement with data reported in [14, 15], although embrittlement has been found to occur at slightly higher swelling levels, between 10% to 20%, in these studies. This indicates that other features

might also influence the transition towards embrittlement. Some of these features, either microstructural or structural, are investigated numerically in Section 3. In order to gain some insights into the fracture physical mechanisms, microstructural observations of selected samples are described in the next section.

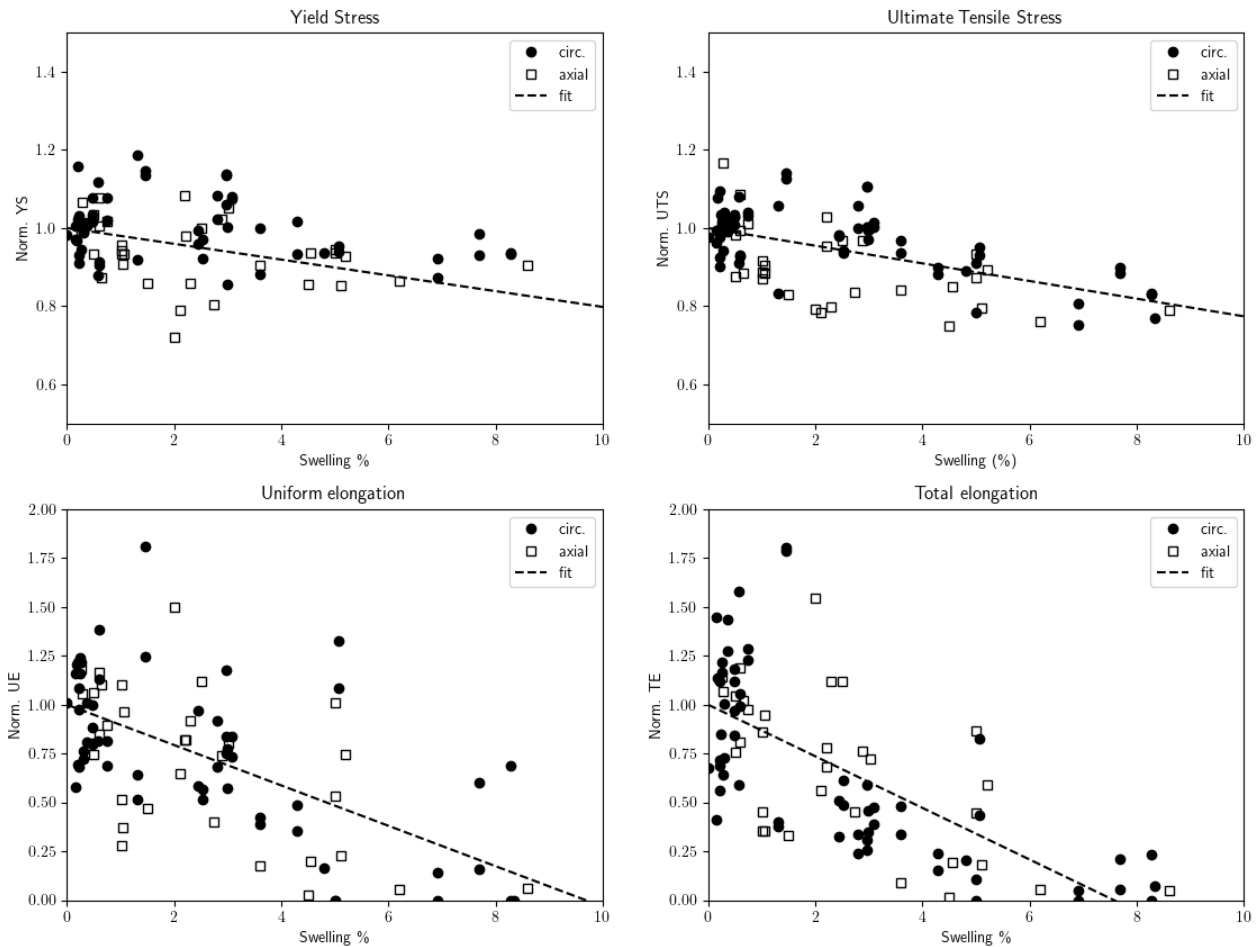


Fig. 5. Normalized tensile properties (Eq. 1) for axial and ring tests as a function of swelling. Dashed lines correspond to a fitted linear function with parameters from Table 2

2.2. Microstructural analysis of embrittlement

TEM and SEM examinations of 15-15Ti ring tensile specimens were performed to investigate irradiation-induced microstructural features and fracture mechanisms, respectively. TEM examinations were carried out with a 300 kV FEI TECNAI 30 G2 TEM (LaB6 gun) equipped with EDS and Gatan Image Filtering (GIF) for EELS and EFTEM analyses. Post-tensile test fractography used a Zeiss FEG-SEM (Supra 55) specially adapted to study highly radioactive samples and equipped with EBSD, EDS and WDS detectors. A detailed account of these observations is beyond the scope of this paper and will be reported elsewhere, but most important results pertaining to the embrittlement mechanisms are detailed in this section. Table 3 summarizes the characteristics of samples examined by SEM and TEM and described hereafter. It should be reminded that swelling depends on both irradiation temperature and dose in a non-linear way [8]. For a given dose, there is a temperature where swelling is maximal (about 400°C for the material used), so that swelling is lower for lower or higher temperature. For a given irradiation temperature, there is a dose range where swelling is very low (the so-called incubation phase) above which swelling increases. This explains the swelling values reported in Table 3, *i.e.*, the difference of swelling between the two last samples having the same irradiation dose can be attributed to the difference of irradiation temperature.

Table 3

Summary of 15-15Ti microstructural examinations on ring tensile specimens taken from three different irradiation programs.

Irradiation program	Sample dose (dpa)	Average irradiation temperature (°C)	Sample swelling (%)	Type of examination
#1	68	471	0.5	SEM & TEM
#2	80	448	3.1	SEM
#2	93	472	4.4	TEM
#3	94	451	5.0	SEM & TEM

TEM images taken at low magnification for three different levels of swelling show the spatial distribution of voids (see Fig. 6) in grain and near the grain boundaries. At 0.5% swelling (Fig. 6(a)), very few voids were observed. At higher swelling, a large number of voids are present (Fig. 6(b,c)), with typical sizes up to few tens of nanometers. More importantly, the spatial repartition of these voids was found to be heterogeneous, where density and size are larger close to grain boundaries as shown in Fig. 6(d).

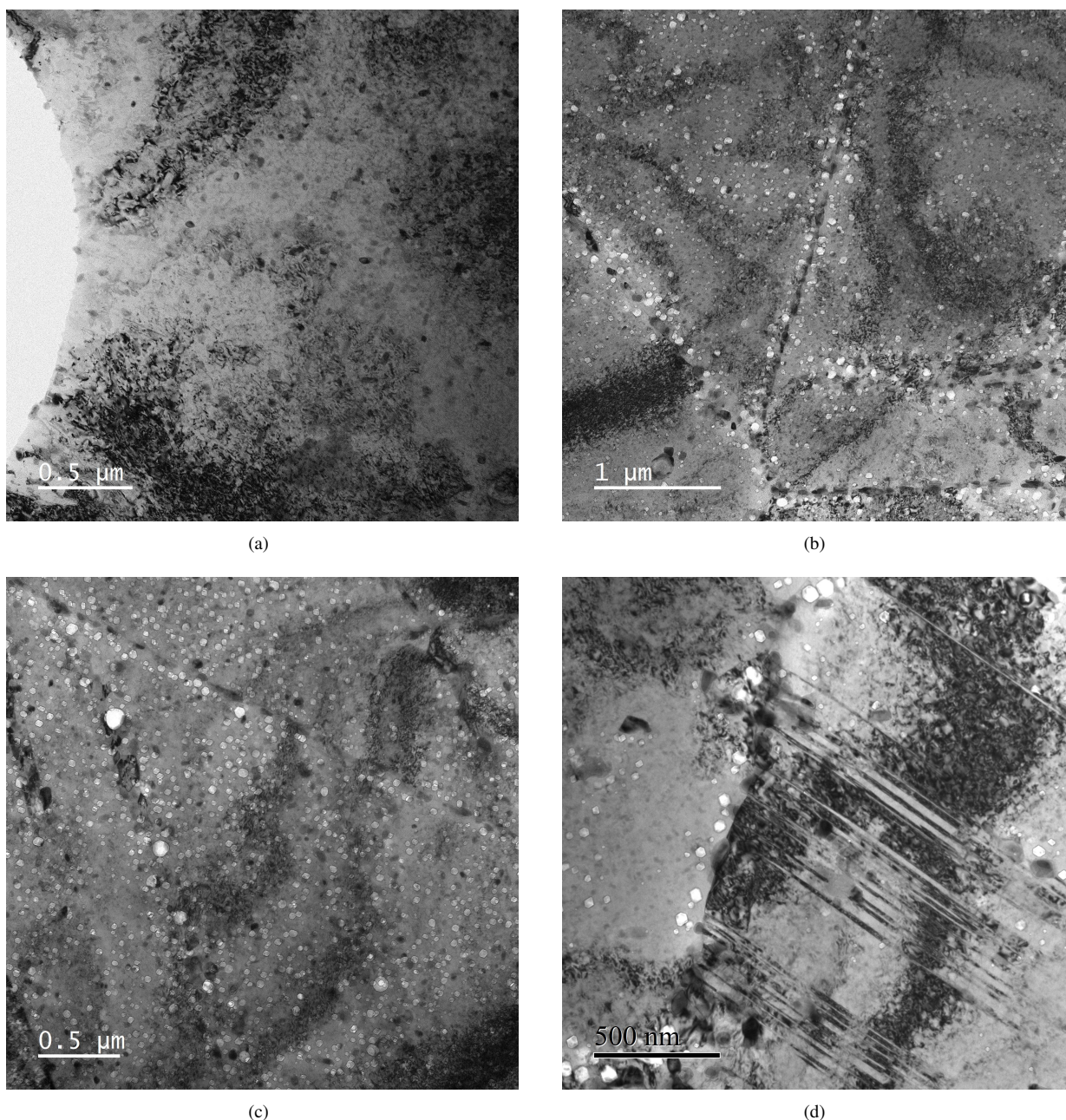
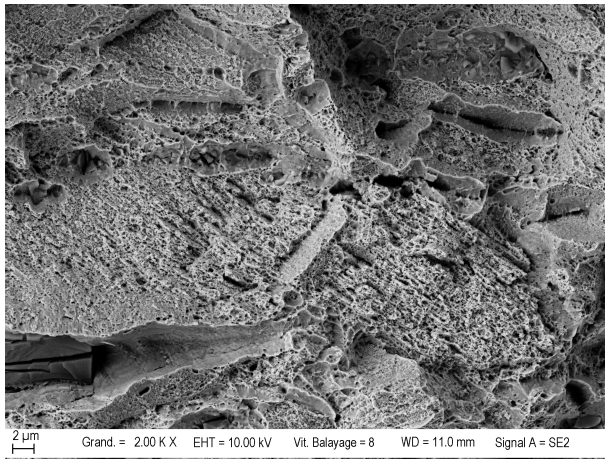
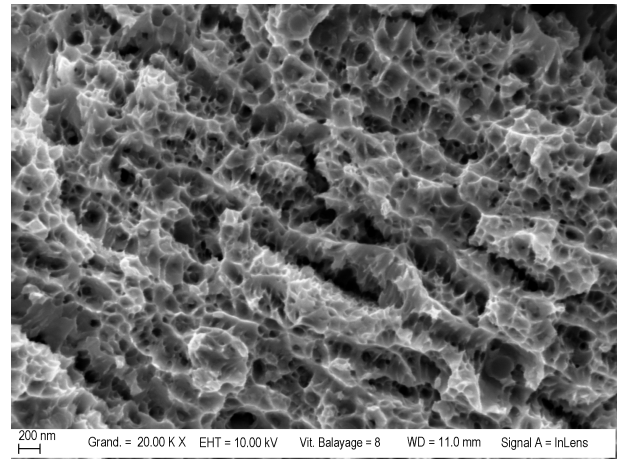


Fig. 6. TEM observations of 15-15Ti irradiated samples with three levels of swelling S : (a) 0.5%, (b) 4.6%, (c) 6%, (d) close up of a grain boundary at $S=4.6\%$.

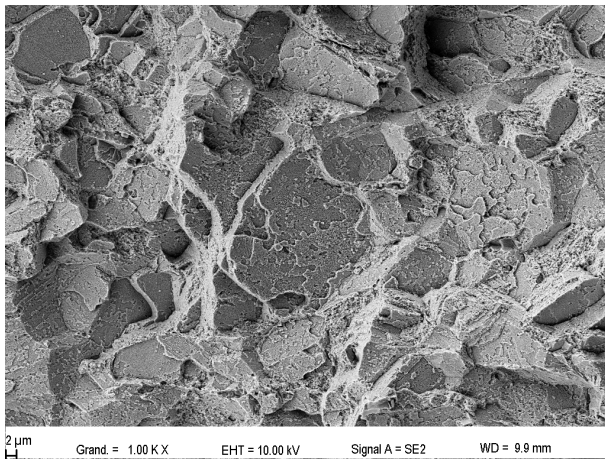
Such enhancement of local porosity adjacent to a grain boundaries was observed in the literature in neutron-irradiated austenitic steels [37] and many irradiated materials [38]. The so-called void-peak zone (VPZ) is often associated with a void denuded zone (VDZ), a region free from cavities, Frank loops or dislocations. In neutron-irradiated austenitic steels, the half width of observed denuded zones ranges from 50 to 100 nm [37], depending on the irradiation temperature, displacement rate, chemical composition and other parameters. TEM observations show also that precipitation is intense in both grains and grain boundaries. Note that most of cavities are attached to precipitates. Preliminary analysis gave indications that these precipitates may correspond to G phase, but additional characterizations (outside the scope of this study) are required. The formation mechanisms of cavities around grain boundaries could also be linked with the well-known radiation-induced segregation (RIS) of elements (mainly Ni and Si) leading to G phase formation at high dose [39, 40]. The effect of RIS is to locally remove Ni and Si from the matrix around grain boundaries, these elements are known to limit the formation of voids in austenitic steels.



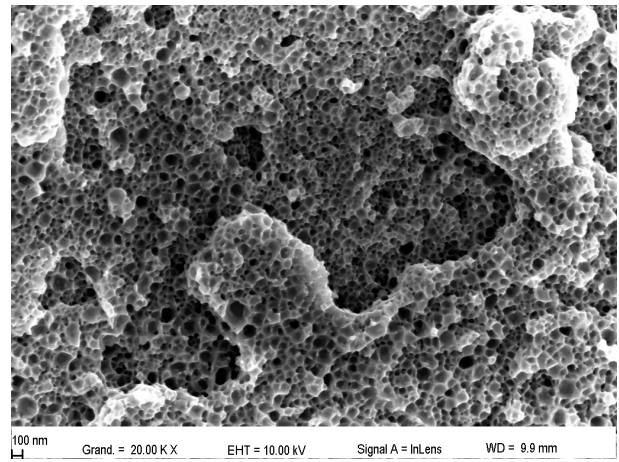
(a)



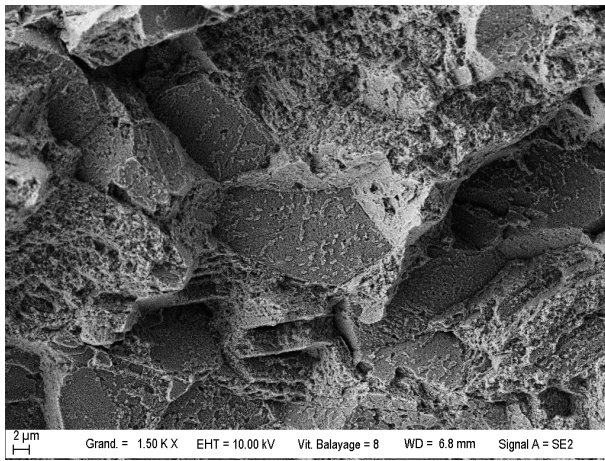
(b)



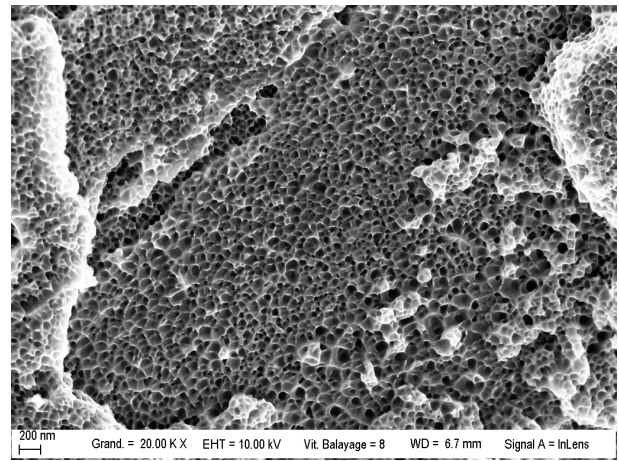
(c)



(d)



(e)



(f)

Fig. 7. SEM observations at two magnifications of 15-15Ti irradiated samples with three levels of swelling after tensile tests at 20°C: **(a and b)** 0.5%, **(c and d)** 4.6%, **(e and f)** 6%.

195 **Fig. 7** shows SEM images of fracture surfaces of ring tensile specimens at two magnifications. In the sample with the lowest swelling level ($S = 0.5\%$, **Fig. 7(a,b)**), fractography reveals a classic transgranular ductile fracture with dimples resulting from nucleation, growth and coalescence of voids originating from intragranular inclusions or secondary phases. At higher swelling ($S > 3\%$, **Fig. 7(c,d,e,f)**), fracture surfaces were still ductile and characterized by the presence of dimples, but with two different features compared to the low swelling case. First, smaller dimples were observed. Second, dimples appear along flat regions, as seen for example on **Fig. 7(e)**, resembling grain boundaries. As TEM observations have shown that voids are in higher density close to grain / twin boundaries, this fracture mode can thus be categorized as "quasi"-intergranular ductile, occurring through irradiation-induced nanovoid growth and coalescence along surfaces parallel to grain / twin boundaries. Regions with transgranular ductile fracture with dimples were also present in the fractography at higher swelling. Finally, at the scale of the specimen, fracture surfaces are slanted with respect to the tensile direction for low swelling levels and become perpendicular for the highest swelling level.

200

In summary, TEM observations associated with SEM fractographies gave some insights into damage and fracture mechanisms occurring during tensile test for high swelling levels:

- Dimpled surfaces parallel to grain (or twin) boundaries as observed in SEM fractography could be associated with the presence of a void "wall" or larger size voids near these boundaries.
- Intense intergranular precipitation was also observed and could contribute to the evolution of damage and void porosity in grain boundaries.
- Regions exhibiting intragranular fracture with dimples observed in fractography could be associated with regions of higher porosity inside grains.

These observations are consistent with the experimental data provided in [15] regarding the transition from slanted to perpendicular fracture surfaces as swelling increases. Remarkably, in both cases, the transition appears when quasi-embrittlement occurs. The physical fracture mechanism is similar to the one described as "nano-dimples fracture" in [32]. Note that the so-called transgranular channel fracture with plate-like appearance was not detected in any of the surfaces examined. This may be related to the fact that this fracture mechanism requires strain localization triggered by the presence of sessile irradiation defects (such as Frank loops), hence lower irradiation temperatures than the ones assessed.

The results presented in this study regarding the swelling-induced embrittlement on neutron-irradiated austenitic stainless steels are in qualitative agreement with the data available in the literature [8]. However, on the one hand quantitative differences exist for the critical swelling above which embrittlement occurs, and on the other hand modelling is required to understand the link between microscopic fracture mechanisms and macroscopic tensile properties. Modelling and simulations described in the next section thus aim at linking microscopic features to macroscopic quantities. In particular, heterogeneous void distribution, observed in this study (Fig. 6) and modelled in [31], and structural effects are assessed in details.

3. Modelling and simulations

In this section, the constitutive equations used to model irradiated stainless steels with a high level of swelling are described. A bifurcation analysis is then presented, showing semi-analytical results regarding the evolution of strength with swelling as well as fracture angle. Finite element simulations on tensile specimens are finally detailed.

3.1. Constitutive equations

The mechanical behavior of austenitic stainless steels with a high level of swelling is modelled as a porous isotropic elastoplastic material. Due to different definitions, the porosity f is not strictly equal to the swelling level S [31, 33]:

$$\left. \begin{aligned} f &= \frac{V_{void}}{V_{mat} + V_{void}} \\ S &= \frac{V_{void}}{V_{mat}} \end{aligned} \right\} \Rightarrow f = \frac{S}{1 + S} \quad (3)$$

where V_{mat} and V_{void} correspond to the volume of the matrix material and void volume, respectively. Porosity is assumed to come only from the presence of nanovoids, and nucleation from inclusions or precipitates is disregarded.

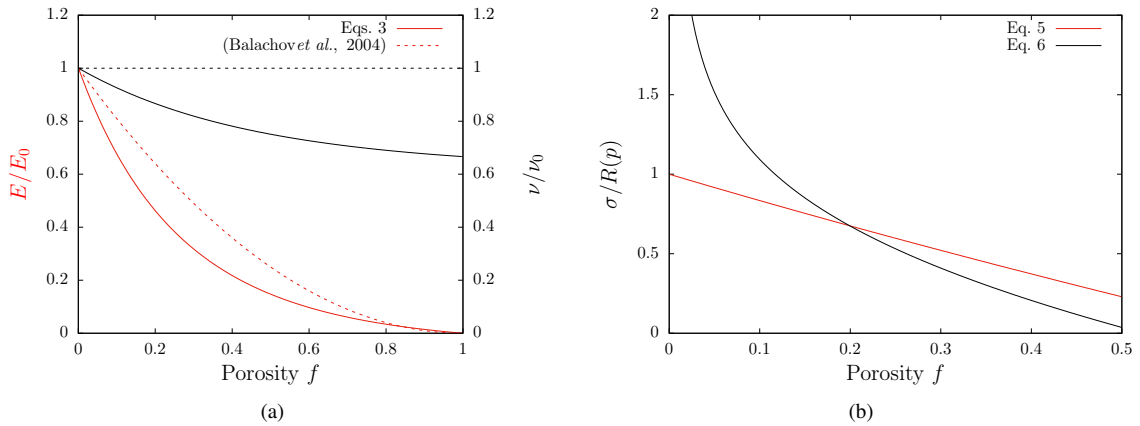


Fig. 8. (a) Evolutions of Young's modulus E and Poisson's ratio ν with respect to porosity f according to Eqs. 4 and [41]. E_0 and ν_0 correspond to the values for $f = 0$. (b) Normalized yield stress in uniaxial loading conditions as a function of porosity, according to Eqs. 5, 6 and 7

The elastic behavior is assumed to follow Hooke's law, with the compression modulus K and shear modulus μ depending on the porosity as [33]:

$$\begin{aligned} K &= K_0 - f \frac{K_0}{1 - (1-f) \frac{K_0}{K_0 + K^*}} & K^* &= \frac{4}{3} \mu_0 \\ \mu &= \mu_0 - f \frac{\mu_0}{1 - (1-f) \frac{\mu_0}{\mu_0 + \mu^*}} & \mu^* &= \frac{\mu_0}{6} \frac{9K_0 + 8\mu_0}{K_0 + 2\mu_0} \end{aligned} \quad (4)$$

from which the Young's modulus $E = (9K\mu)/(3K + \mu)$ and Poisson's ratio $\nu = (3K - 2\mu)/(6K + 2\mu)$ can be obtained. For $f = 0$, $[K, \mu] = [K_0, \mu_0]$. The evolutions of Young's modulus and Poisson's ratio with respect to the porosity are shown in Fig. 8(a). For the former, the evolution is in qualitative agreement with the experimental results and model proposed in [41] where both Young's modulus and shear modulus are assumed to follow a $(1-f)^2$ law. In the following, the values of E_0 and ν_0 - corresponding to $f = 0$ - are set to 200GPa and 0.3, respectively.

Two equivalent stresses $\sigma_{eq}^{g,c}$ are defined to model the plastic behavior in presence of porosity. The first one comes from the Gurson-Tvergaard-Needleman (GTN) model [42, 43]:

$$\sigma_{eq}^g \quad \text{such as} \quad \left(\frac{\sigma_{vM}}{\sigma_{eq}^g} \right)^2 + 2qf \cosh\left(\frac{3}{2} \frac{\sigma_m}{\sigma_{eq}^g} \right) - 1 - q^2 f^2 \stackrel{\text{def.}}{=} 0 \quad (5)$$

with $\sigma_{vM} = \sqrt{[3/2] s : s}$ the von Mises equivalent stress and $\sigma_m = \text{trace}(\boldsymbol{\sigma})/3$ the mean stress, with $\boldsymbol{\sigma}$ the Cauchy stress tensor and $s = \boldsymbol{\sigma} - \sigma_m \mathbf{I}$ the stress deviator. q is a numerical parameter introduced to improve the accuracy of the model, and sets to $q = 1.5$ in the following [44]. The GTN model is an extension of the Gurson model [23] obtained through the rigorous micromechanical analysis of a hollow sphere, and is widely used to describe the plasticity of porous materials for low porosity / void growth deformation regime (Fig. 9). The validity - and limits - of the GTN model have been assessed extensively in the literature [44].

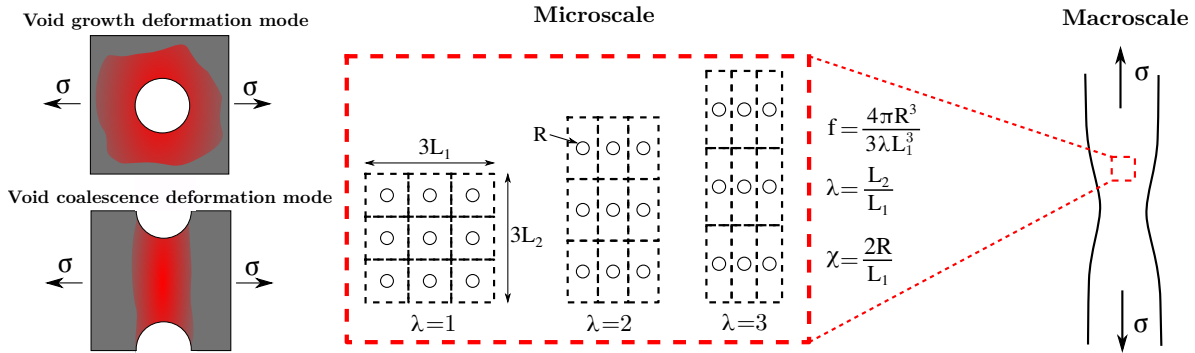


Fig. 9. Micromechanical modelling of porous materials: Homogenization of an array of spherical voids and definition of the geometrical parameters f , λ and χ

A second equivalent stress is defined:

$$\sigma_{eq}^c \quad \text{such as} \quad \sigma_I \stackrel{\text{def.}}{=} \left[(1 - \chi^2) \left(0.1 \left(\frac{\chi^{-1} - 1}{W} \right)^2 + 1.2 \sqrt{\chi^{-1}} \right) \right] \sigma_{eq}^c \quad (6)$$

that is the homogenized model relevant for large porosity where plastic flow is no longer diffuse but localizes in between adjacent voids [44]. σ_I is the component of the stress perpendicular to the localization plane, W is the void aspect ratio and χ is related to the intervoid distance (Fig. 9). Finally, the yield criterion of the material is defined as:

$$\mathcal{F} = \max(\sigma_{eq}^g, \sigma_{eq}^c) - R(p) \quad (7)$$

where $R(p)$ represents the isotropic hardening, with p a measure of the accumulated plastic strain in the matrix material surrounding voids. $\mathcal{F} < 0$ corresponds to elasticity, and plasticity occurs for $\mathcal{F} = 0$. As an example, in the case of uniaxial loading conditions, the value of the non-zero component of the stress tensor σ for which plasticity will occur according to Eqs. 5, 6 and 7 is shown on Fig. 8(b). For low porosity, plasticity comes from Eq. 5, *i.e.*, void growth diffuse plasticity. For large porosity, plasticity occurs from Eq. 6, *i.e.*, void coalescence localized plasticity.

Plastic flow is defined assuming normality rule [45]:

$$\dot{\boldsymbol{\epsilon}}_p = (1 - f) \dot{p} \frac{\partial \mathcal{F}}{\partial \boldsymbol{\sigma}} \quad (8)$$

For $f \rightarrow 0$, *i.e.*, no porosity, Eqs. 5, 6, 7, 8 reduce to classical von Mises plasticity. The model described hereabove is in fact the simplest homogenized model for porous materials including both growth and coalescence regime, and corresponds to a particular case of refined models described for example in [44]. Such kind of homogenized models have

been extensively discussed in the literature through comparisons to reference finite element simulations where voids are modelled explicitly [44]. The model described here shares some features with the modelling proposed by Margolin and coauthors in [30, 32]: the Rice-Tracey law used to compute the evolution of porosity is recovered by the Eqs. 5, 7 and 8. The main difference is the modelling of void coalescence which comes here (Eq. 6) from a rigorous micromechanical analysis of porous materials [24].

For simplicity, voids are assumed in the following to remain spherical ($W = 1$), and the simplest isotropic linear hardening law is considered:

$$R(p) = R_0 + H p \quad (9)$$

To summarize, the model requires only four input parameters: $\{R_0, H\}$ to characterize the hardening behavior of the matrix material surrounding voids, and $\{f, \lambda\} = \{f_0, \lambda_0\}$ to describe the initial void distribution. Note that calibrating other parameters may be necessary to get predictions in quantitative agreement with experimental data, such as the q value used in Eq. 5, but the main idea of the model is to identify key parameters. R_0 can be seen as a normalizing factor for stresses, and can be set to an arbitrary value without loss of generality. In what follows, $R_0 = 800$ MPa is used. The initial porosity value is related to the swelling level according to Eq. 3. The parameter λ^2 is a simple way to describe the anisotropy of void distribution observed experimentally (Figs. 1(a), 6). Voids are assumed to be aligned along the principal axis set by the loading direction, as shown on Fig. 9, which is clearly a simplified approach. Again, the model is set as the minimal physically-based one allowing to assess key parameters. Finally, it should be noticed that void size is not accounted for in the model as only dimensionless parameters are used (Fig. 9). This classical assumption in ductile fracture / porous materials modelling [44] holds in particular when void size is large compared to the typical lengthscale sets by dislocation density ρ ($\ell \sim \sqrt{\rho}^{-1}$) [27]. Absence of void size effects has been confirmed experimentally in [28] for conditions close to the one considered in this study. The constitutive equations described in this section have been implemented in the MFront code generator [47] under finite strain in order to be used in finite element simulations. The numerical implementation has been described in detail elsewhere [48].

3.2. Theoretical predictions

Semi-analytical predictions regarding the evolution of mechanical properties with swelling can be obtained with the model described in the previous section neglecting structural effects (induced by the geometry of the test samples) and assuming that the hardening is weak. In that case, Eqs. 5, 6, 7 can be used to obtain the maximal stress that the material can sustain under tensile loading, which is simply the stress for which plasticity will occur³. The dependence of this maximal stress with respect to the swelling level S and to the heterogeneity of void distribution λ is shown on Fig. 10(a). Two separate regions exist, where plasticity is driven either by void growth diffuse plasticity (Eq. 5) or void coalescence localized plasticity (Eq. 6). For very high swelling level and / or highly heterogeneous void distribution, the maximal stress goes to zero: the material can not sustain any mechanical loading as voids are interconnected. This is consistent with the experimental observations of failures of FBR fuel claddings or wrappers simply by manipulating them [14, 15].

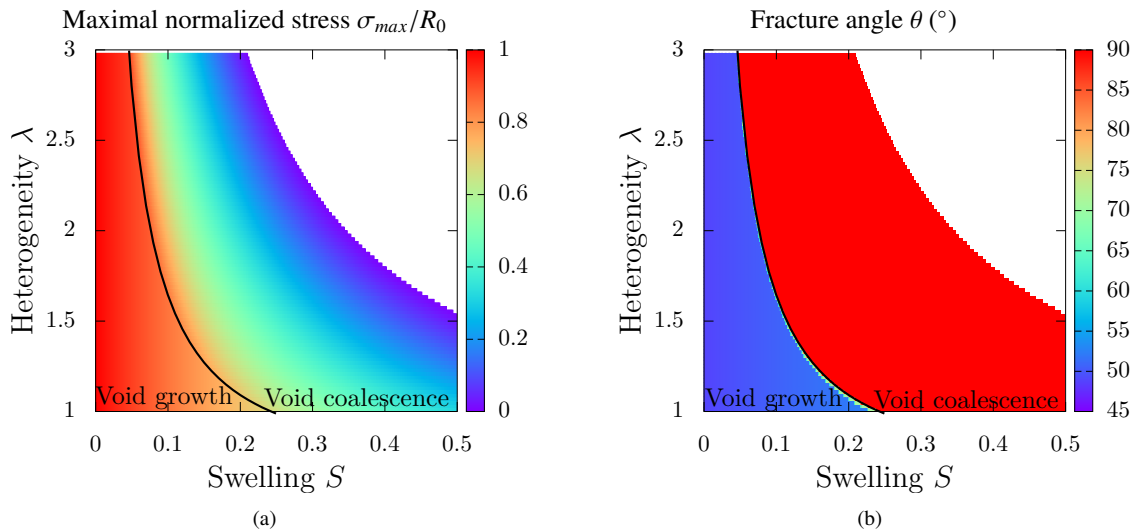


Fig. 10. Theoretical predictions of (a) maximal tensile stress and (b) fracture angle (see Inset Fig. 11) with respect to the loading direction as a function of swelling level S and void distribution heterogeneity λ (defined in Fig. 9), for uniaxial tensile loading conditions. The black line corresponds to the transition from void growth plasticity (Eq. 5) to void coalescence plasticity (Eq. 6).

Moreover, it is possible to perform a bifurcation analysis of the constitutive equations described by Eqs. 5, 6, 7, 8 as initially proposed in [29] for the Gurson model and performed in [49] for the GTN model. The principle of such

²It should be noted that the parameter λ , as f , evolves under mechanical loading. The evolution law simply comes from geometry (Fig. 9), and can be found for example in [46].

³Without hardening, the ultimate tensile strength is equal to the yield stress.

analysis, theoretically described in [50], is to evaluate if, from a homogeneous deformation / stress state, a heterogeneous deformation / stress state can occur in the form of a localized band (Inset of Fig. 11(a)). The occurrence of such strain localization is often used as an indicator of fracture strain and crack path at the material scale. In practice, for a given set of constitutive equations, and for a given loading, the condition for strain localization inside a band is:

$$H \quad \text{such as} \quad \mathcal{I} = \det(\mathbf{n} \cdot \mathbf{C}(f, H, \lambda) \cdot \mathbf{n}) = 0 \quad (10)$$

where \mathbf{C} is the incremental stiffness fourth order tensor relating stresses and strains increments $\dot{\boldsymbol{\sigma}} = \mathbf{C} : \dot{\boldsymbol{\epsilon}}$, and \mathbf{n} is the normal to the localization band (Fig. 11(a)). The expression of \mathbf{C} for the constitutive equations used here is given in Appendix A. Fig. 11(a) shows, for two porosities and uniaxial loading conditions and no hardening $H = 0$, the evolution of \mathcal{I} as a function of the localization band angle θ . For the lowest porosity, \mathcal{I} is always higher than zero, *i.e.*, bifurcation cannot occur, contrary to the case of high porosity. The influence of decreasing the hardening parameter is mainly to shift the curves downwards. In practice, for tensile loading conditions and fixed values of porosity and void heterogeneity λ , the angle θ for which \mathcal{I} is minimal is looked for, corresponding to the orientation of the band. The value of H is then determined in order to have $\mathcal{I}(\theta, H) = 0$.

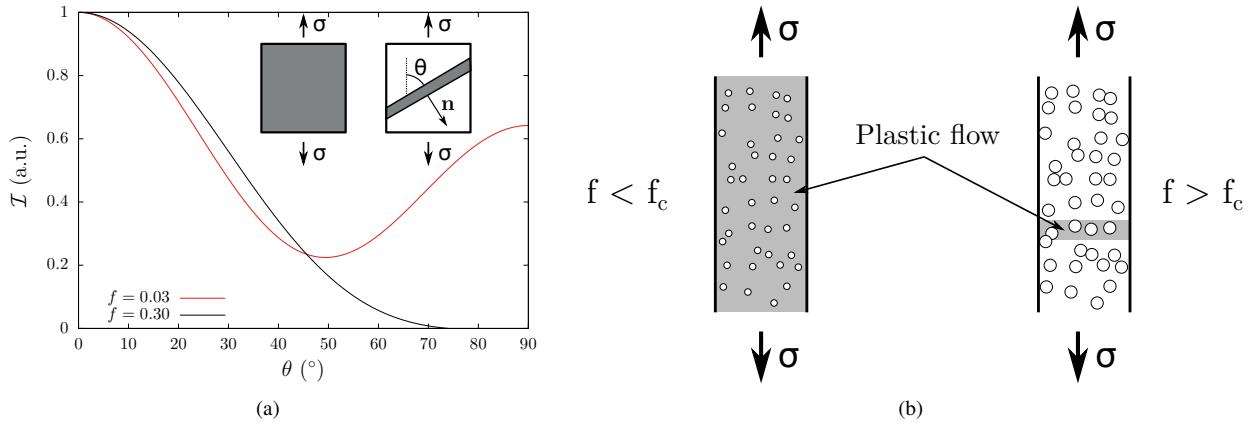


Fig. 11. (a) Evolution of the bifurcation indicator \mathcal{I} (Eq. 10) as a function of the band angle θ (Inset) for uniaxial loading conditions, $H = 0$, $\lambda = 1$ (b) Occurrence (or not) of strain localization at the material scale depending on the porosity

The results of this analysis are twofold. First, in the void growth regime (Fig. 10(b)), Eq. 10 can not be satisfied for any value of θ for any positive value of the hardening modulus. The lowest value is obtained for $\theta_{min} \approx 50^\circ$. In this regime ($f < f_c$ Fig. 11(b)), no strain localization happens. The occurrence of necking eventually changes the mechanical loading conditions, and allows satisfying Eq. 10, as shown in [49], and thus fracture is expected to occur for $\theta_f \approx \theta_{min}$. Secondly, in the void coalescence regime, Eq. 10 is satisfied as soon as the hardening modulus is lower than a critical value, associated with $\theta = 90^\circ$ (Fig. 11(b)). Thus, as soon as plasticity occurs in a structure under tensile loading, strain localization appears in a band perpendicular to the loading direction. High levels of plastic strain can still be achieved in the band prior to fracture, but the macroscopic behavior will appear brittle.

The theoretical predictions shown in Fig. 10 are consistent with the experimental observations, and indicate that the decrease of strength and quasi-embrittlement observed in irradiated austenitic stainless steels with a high level of swelling can be understood solely by the presence of voids. In particular, the embrittlement results from the transition from void growth to void coalescence regime (Fig. 10), the latter resulting in an unstable deformation mode (Fig. 11). The effect of void distribution inhomogeneity on tensile strength and critical porosity / swelling above which embrittlement occurs is strong, and may explain the differences observed between sets of experimental results. However, the mechanical properties measured experimentally may deviate from these predictions because of structural effects induced by the geometry of the test specimens - as reported in [15] and / or because of inhomogeneity of the void distribution at the scale of the test specimen. To assess these effects, finite element simulations are required.

3.3. Finite element simulations

Mechanical tests on fuel claddings are often performed on ring tensile specimens (Fig. 12(a)) as presented previously in the database. Finite element simulations of tensile tests on ring specimens are thus described in this section, and the results are discussed in Section 4. The finite element mesh used is shown on Fig. 12(b): quadratic elements with full integration are used. The convergence with respect to mesh size has been checked for all results presented hereafter. A prescribed displacement is imposed to the inner mandrel, and frictionless contact is considered between the mandrel and the specimen. Simulations are performed using Cast3M finite element solver [51]. In addition, simulations are also performed for comparisons on flat tensile specimens having the same geometrical parameters - thickness, width, gage length - than the ring tensile specimens.

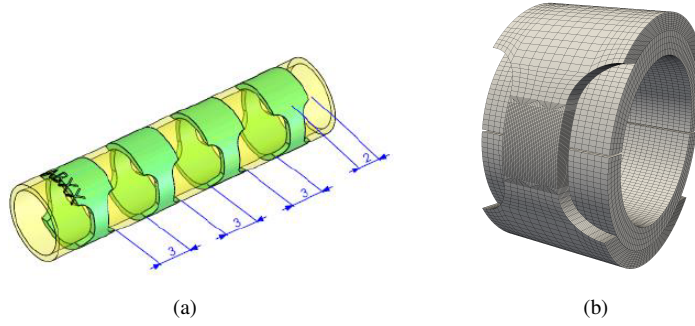


Fig. 12. (a) Sampling of ring tensile specimens from FBR fuel claddings (b) Mesh used for the finite element simulations (due to symmetries, only one eight of the mesh is actually used)

The typical output of the simulation - conventional strain-stress curves as in the experiments (Fig. 1(b)) - is shown in Fig. 13(a), allowing computing conventional tensile properties: yield stress at 0.2% plastic strain YS, ultimate tensile strength UTS and associated plastic strain UE, and plastic fracture strain TE. YS and UE are sensitive to the initial gap between the ring tensile specimen and the mandrel, as well as to friction coefficient. Therefore, only UTS and TE are used in the following to assess the influence of swelling, which is justified based on the experimental results as they display the same trends as YS and UE.

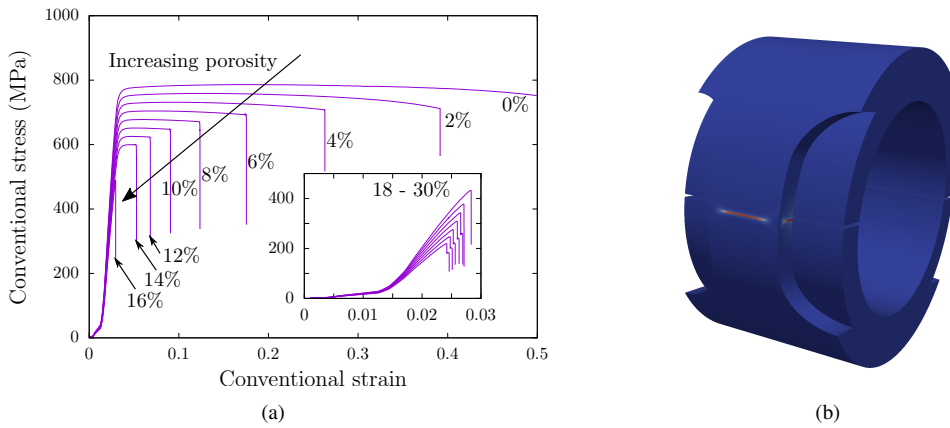


Fig. 13. (a) Conventional stress-strain curves obtained on ring tensile specimens for $H = 850\text{MPa}$, $\lambda = 1$, for porosity ranging from 0% to 30% (every 2%) (b) Accumulated plastic strain field p close to fracture for $f = 20\%$

Accumulated plastic strain fields (Fig. 13(b)) allow to monitor the occurrence of strain localization. For the set of simulations on Fig. 13(a), one can already see that, the higher the swelling, the lower the stress the sample is able to sustain. The fracture strain also decreases drastically as swelling increases, up to a point where failure occurs in the elastic regime. These observations, in qualitative agreement with the experimental data, are assessed in more details and compared in the next section.

4. Numerical results

The results of the finite element simulations are detailed in this section, firstly for the effect of materials parameters to support the theoretical results (Fig. 10), and secondly for the structural effects.

4.1. Effects of material parameters

Fig. 14 shows the effects of the matrix hardening parameter H and the inhomogeneity of void distribution λ on conventional stress-strain curves. As expected, the hardening has a slight effect on the mechanical strength (Fig. 14(a)) for low values of porosity: the higher the hardening modulus, the higher the tensile strength. This can be understood using the Considère's criterion [52] stating that the maximal force during a tensile test occurs when $d\sigma/dp = \sigma$, leading to $\sigma = H$ for the linear hardening considered here (Eq. 9). The effect of hardening - for the two values considered - on fracture strain is however very weak. For a given value of hardening, the effect on the inhomogeneity of void distribution λ is however stronger on the fracture strain, as shown on Fig. 14(b). Especially, the porosity threshold for which fracture occurs in the elastic regime is about 16% for $\lambda = 1$, and reduced to about 6% for $\lambda = 2$.

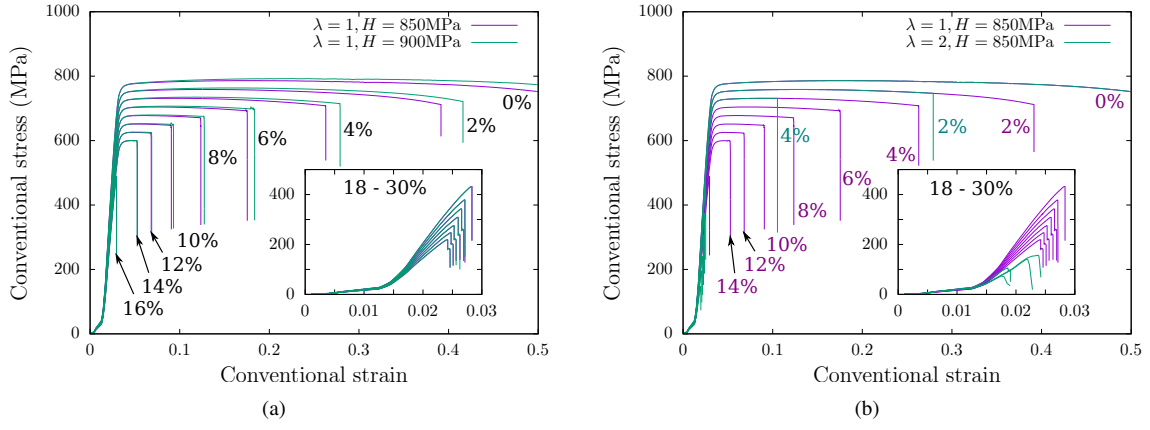


Fig. 14. Conventional stress-strain curves obtained on ring tensile specimens for porosity ranging from 0% to 30% (every 2%), as a function of (a) matrix hardening H and (b) void distribution inhomogeneity λ

The evolutions of conventional tensile properties UTS and TE - extracted from these stress-strain curves - with respect to swelling are shown on Fig. 15. Tensile strength decreases with swelling, with a weak effect of matrix hardening and strong effect of void distribution inhomogeneity (Fig. 15(a)). A slope break is observed for a critical swelling above which maximal stress decreases faster. This is consistent with the theoretical predictions (Fig. 10(a)) where the critical swelling is associated with the transition from void growth to void coalescence deformation mechanism. The evolution of the normalized plastic fracture strain with respect to swelling is plotted on Fig. 15(b), showing the occurrence of critical swelling above which $TE = 0$, *i.e.*, fracture occurs in the elastic regime. Both critical swelling identified on Fig. 15(a) and Fig. 15(b) have the same values, which is again in accordance with the theoretical predictions stating that void coalescence deformation mode leads to strain localization.

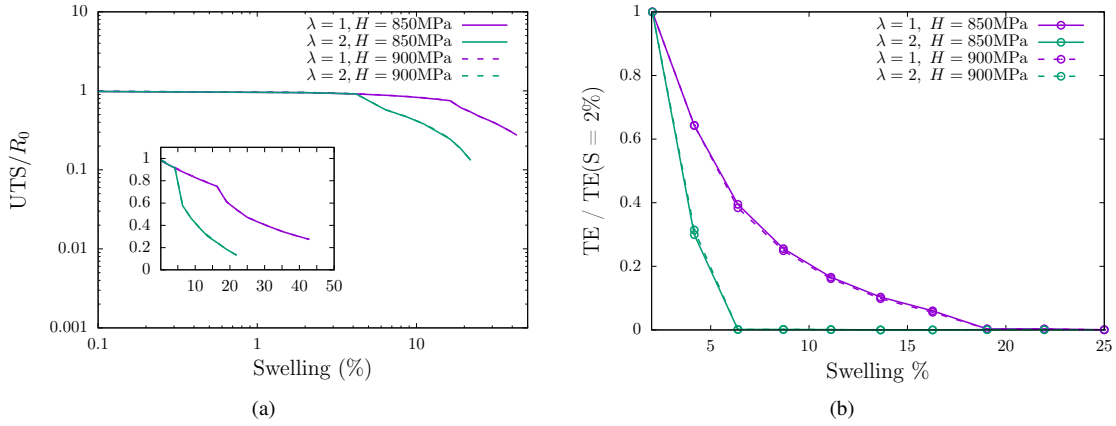


Fig. 15. Evolution of (a) tensile strength and (b) plastic fracture strain as a function of swelling, for different values of matrix hardening H and void distribution inhomogeneity λ , for ring tensile specimen

More quantitatively, the critical swelling in these numerical simulations are $S_c(\lambda = 1) \approx 18\%$ and $S_c(\lambda = 2) \approx 6\%$, lower than the ones obtained in Fig. 10 (about 24% and 8%, respectively). This potentially indicates the presence of structural effects that are assessed in the next section.

4.2. Structural effects

Results of numerical simulations performed on flat tensile specimens are compared to the previous one obtained on ring tensile specimens (Fig. 16). For all sets of material parameters (H , λ), a significant effect of specimen geometry is observed. Mainly, the critical swelling level is higher for the flat tensile specimens than for ring tensile specimens, delaying the steeper decrease of tensile strength (Fig. 16(a)) and fracture (Fig. 16(b)). Results from Fig. 16(a) for flat tensile specimens are in quantitative agreement with the theoretical analysis (Fig. 10). The structural effect can be understood as follows (as proposed earlier in [15]). Due to the ring tensile geometry, a stress gradient is present along the thickness for low values of strain (typically at the macroscopic yield point). Higher stresses are experienced at the inner surface of the ring, and local yielding occurs there before extending to the outer surface. Accumulated plastic strain are also higher at the inner surface, leading to higher increase of porosity. For initial porosity close to the transition from void growth to void coalescence plasticity, this effect may be sufficient to trigger locally void coalescence at the inner surface, resulting in lower tensile strength and fracture strains (Fig. 16). This structural effect is consistent with the experimental results presented in [15] showing delayed embrittlement for flat tensile specimens compared to ring tensile specimens. However, it should be noted that the results were obtained on different materials, and the difference observed can also be the result of different void distribution inhomogeneity (Fig. 15).

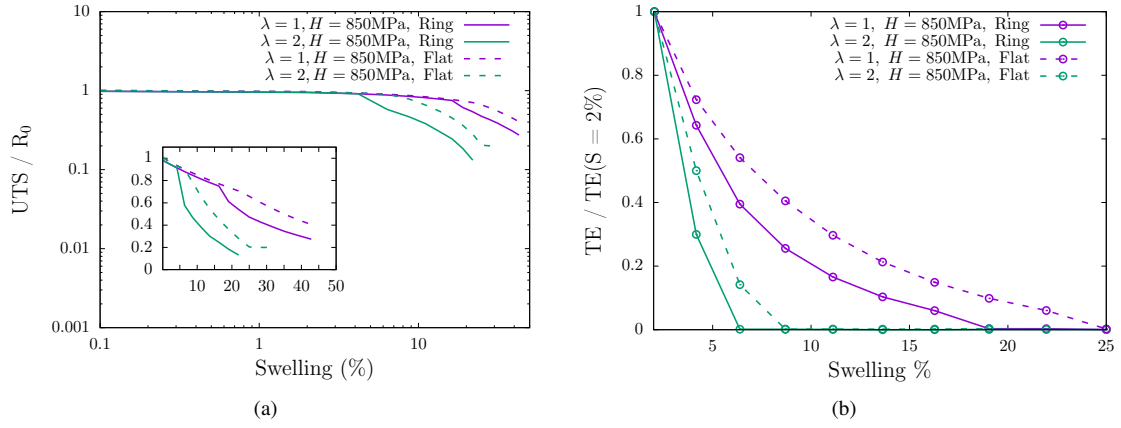


Fig. 16. Evolution of (a) tensile strength and (b) plastic fracture strain as a function of swelling, for different values of matrix hardening H and void distribution inhomogeneity λ , for ring and flat tensile specimens

Another structural effect put forward in [15] to explain the differences between tests on ring and flat specimens is the presence of a swelling gradient along the thickness. This effect will be assessed in Section 5.

370 4.3. Comparisons to experimental results

The analytical and numerical results are compared to the experimental results in this section. The evolutions of ultimate tensile strength and total elongation as a function of swelling obtained in Section 2.1 are shown in Fig. 17 along with numerical results on ring tensile specimens. Experimental results are presented using the calibrated functions (Eq. 2) with parameters from Table 2. For both ultimate tensile strength and total elongation, the experimental trends are correctly described by the numerical results for weakly heterogeneous void distributions $\lambda \in [1 : 2]$. In particular, the initial slopes (for small values of swelling) are well predicted. Moreover, the fact that heterogeneous void distribution $\lambda > 1$ is needed to capture the critical swelling level above which quasi-embrittlement occurs (Fig. 17(b)) is consistent with TEM observations (Fig. 6). These comparisons support the fact that void distribution is a key factor for embrittlement of neutron-irradiated austenitic stainless steels.

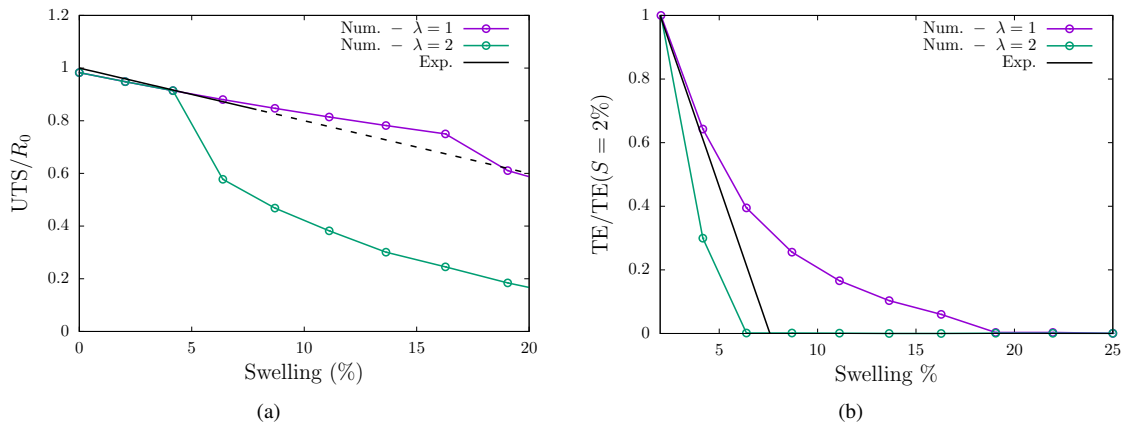


Fig. 17. Evolution of (a) tensile strength and (b) plastic fracture strain as a function of swelling, for different values of void distribution inhomogeneity λ , for ring specimens. Black solid lines correspond to experimental data (Eq. 2 and Table 2), and dashed lines to the prolongation of these linear functions above the maximal swelling on which they were calibrated.

380 Experimental results presented in Section 2.1 are limited to swelling values below or close to the embrittlement limit, and do not allow to assess the regime where strength decreases drastically. Experimental data provided in [15, 8] are thus used and compared to the analytical and numerical results in Fig. 18. First, Fig. 18(a) shows the evolution of the fracture angle as a function of swelling obtained experimentally compared to the analytical predictions from Fig. 10(b). The transition from slanted to perpendicular fracture surface is correctly predicted by the model, and the comparison to the experimental data indicates that quantitative agreement is found for a heterogeneous void distribution characterized by $\lambda \approx 2$. Thus, this value is used to compare the evolution of tensile strength predicted by the simulations on ring and tensile specimens to two sets of experimental results in Fig. 18(b). Interestingly, the differences observed in [15, 8] for the two datasets [15, 8] and explained, at least partially, by the difference of test geometry is supported by the simulations performed in this study. This points out the importance of the tensile test geometry to evaluate the embrittlement limit, 390 which will be discussed in the following.

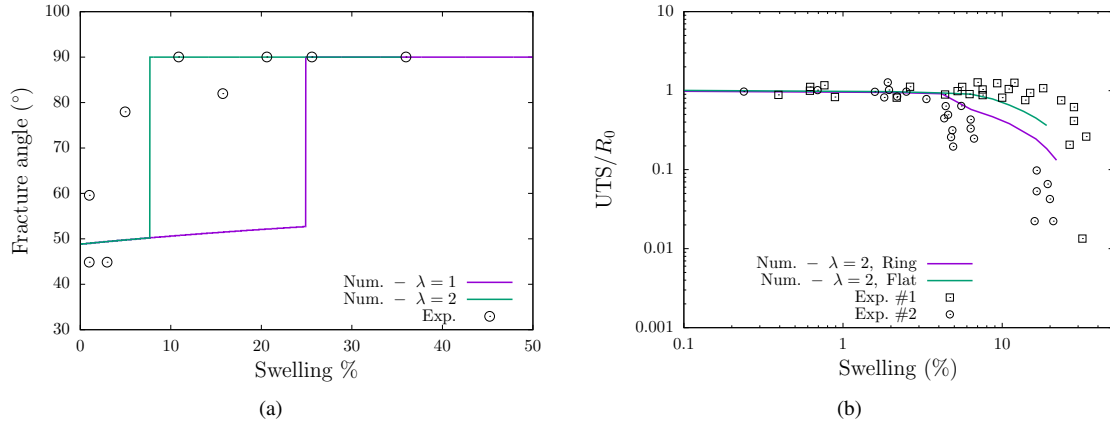


Fig. 18. Evolution of (a) fracture angle predicted by the analytical model and (b) tensile strength predicted by numerical simulations as a function of swelling, for different values of void distribution inhomogeneity λ , for ring and flat tensile specimens. Experimental data correspond to values reported in [15, 8], where the two datasets (#1,#2) correspond to flat tensile and ring test geometry, respectively.

These comparisons indicate that differences of test geometry, as proposed in [15], but also of void distribution may explained the quantitative differences observed in the literature regarding the embrittlement limit. Another factor is the presence of swelling / porosity gradient in test specimens that is assessed numerically in the next section.

5. Discussion

395 The numerical results presented in Section 4 correspond to the case of an homogeneous porosity in the tensile specimen, focusing on assessing the key parameters involved in the occurrence of the quasi-embrittlement. In this section, the effect of inhomogeneous porosity is first studied, in order to be closer to experimental observations. Then, practical guidelines are discussed with respect to the interpretation of experimental tests and on the determination of the parameters of the constitutive equations.

400 5.1. Effect of porosity gradient

Due to the presence of temperature gradient through the thickness of fuel claddings used in FBR applications, local swelling gradients have been reported in the literature [7]. However, the swelling levels reported in experimental studies are measured mostly through density measurements, hence correspond to average values. The effect of the presence of porosity gradient on the tensile properties measured from ring tensile specimens is assessed in this section. The porosity f is assumed to vary linearly through the thickness h :

$$f(z) = \max \left[\frac{\nabla f}{h} \left(z - \frac{h}{2} \right) + f_0, 0 \right] \quad (11)$$

The corresponding macroscopic (average) swelling level can be computed using Eqs. 3, 11:

$$S = \frac{1}{h} \int_0^h \frac{f(z)}{1 - f(z)} dz \quad (12)$$

$\nabla f = \pm[0.1, 0.2]$ are used in the following. These values have been taken voluntarily large - the worst case corresponding to the absence of swelling on one side and 25% on the other side - to exacerbate the potential effects. Experimental results shown in [7] are closer to $\nabla f = 0.1$. It should also be noted that, contrary to what have been proposed in [15] to explain the geometry effects - that the swelling is higher at the inner surface - swelling gradients can be either positive or negative. Irradiation temperature is always higher at the inner surface, but the sign of the gradient depends if the inner temperature is higher or lower than the temperature for which swelling is maximal. In the former case, swelling gradient will be negative, while positive in the latter case.

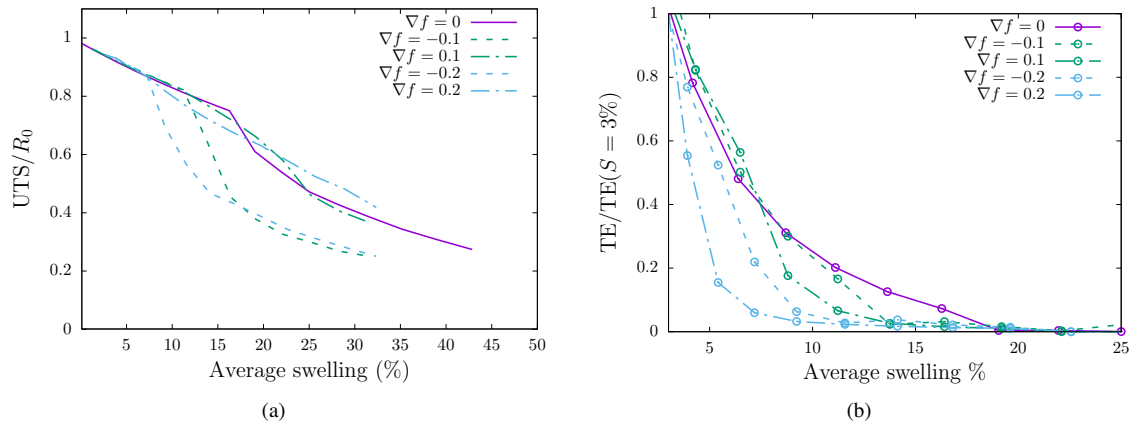


Fig. 19. Evolution of (a) tensile strength and (b) plastic fracture strain as a function of average swelling, for ring shape specimen, $H = 850\text{MPa}$ and $\lambda = 1$, for different values of the swelling gradient ∇f (Eq. 11)

The effect of such gradient is shown on Fig. 19 on the tensile strength and fracture strain, as a function of the average swelling (Eq. 12). In all cases, the presence of gradients - either positive or negative - leads to a decrease of the critical swelling above which failure occurs in the elastic regime. Higher local porosity can trigger void coalescence deformation regime in which the local stress decreases quickly with strain, hence leading to lower stress. Moreover, the decrease is more significant when the gradient is negative, *i.e.*, the porosity is higher in the inner surface of the ring. For low applied macroscopic strain, higher local strain are experienced at the inner surface of the ring due to bending of the specimen. Thus, stress decreases more quickly in cases where the porosity is higher at the inner surface than at the outer surface. The effect of swelling gradient on ring tensile specimen is thus to exacerbate the structural effects observed in Fig. 16.

5.2. Interpretation of experimental tests

Theoretical predictions and numerical simulations reported in the previous sections support the idea that the quasi-embrittlement observed in irradiated austenitic stainless steels with a high level of swelling comes from the transition from a diffuse deformation mode to a localized one at the local scale. The material is still ductile, but strain localization induced by void coalescence deformation regime leads to a brittle behavior at the macroscopic scale, as deformation localizes in one layer of void. Hence, assuming that locally fracture occurs for a critical strain ε_f^{micro} , the macroscopic strain to failure of a tensile sample of length L is $\varepsilon_f^{macro} = (R/L)\varepsilon_f^{micro} \ll 1$, as $R/L \ll 1$, R being the void size. The critical swelling level S_c above which quasi-embrittlement is observed to depend mainly on void distribution (in-)homogeneity: the embrittlement occurs later for homogeneous distribution that corresponds to the upper-bound of the critical swelling. The parameter λ used in this study to characterize this inhomogeneity (observed in Fig. 1(a) where higher density of nanovoids are found at or close to grain boundaries) might be difficult to estimate quantitatively from TEM observations, thus the determination of S_c relies ultimately on mechanical tests. However, care should be taken as structural effects may occur. The evaluation of S_c on ring tensile specimens is expected to lead to a lower bound estimation, as shown in Fig. 16. Similarly, the presence of swelling gradient leads to lower bound estimates of S_c (Fig. 19). In order to calibrate the constitutive equations described in Section. 3.1, it is thus proposed to perform tensile tests on flat specimens, or on ring tensile specimens without swelling gradient. For very low swelling levels, the matrix hardening can be calibrated, and the parameter λ can be estimated based on the critical swelling level S_c by using for example Fig. 10. Hence the model is fully calibrated, and can be used to perform numerical simulations in more complex situations, such as pre-cracked samples in order to evaluate fracture toughness. It should be noted finally that other features might be necessary to be accounted for in the modelling to get quantitative predictions, as detailed in the next section.

6. Conclusion

Austenitic stainless steels used for FBRs claddings experience high irradiation doses at high temperatures, leading to the so-called swelling phenomenon. The mechanical properties depend on the swelling level, and it has been reported in the literature that failure occurs in a brittle-like manner above a critical swelling level. In this study, an additional experimental database of conventional tensile properties versus swelling values - along with SEM and TEM observations - has been described, coming from mechanical tests performed on cold-worked 15-15Ti fuel claddings irradiated in the FBR Phénix. The database, consistent with previous data, shows the decrease of yield stress and mechanical strength as swelling increases, as well as the occurrence of a critical swelling above which a quasi-brittle behavior is observed. A micromechanical analysis of the quasi-embrittlement of irradiated stainless steels experiencing high swelling has been proposed in order to assess the key parameters involved in this phenomenon.

The main outcomes of this study are the following. First, master-curves have been proposed to fit the entire database for the dependence of the mechanical properties to the swelling level. Finite element simulations of the tensile tests on both ring and flat tensile specimens have been performed, using constitutive equations relevant to model porous materials. Simulation results allow to recover the experimental results, *i.e.*, decrease of yield stress / ultimate tensile strength with swelling, as well as the occurrence of the quasi-embrittlement. For a given swelling, the heterogeneity of void distribution

- observed in TEM images - is shown to have a major effect on the quasi-embrittlement. The finite element analysis is supported by a theoretical analysis, predicting the maximal stress and fracture angle as a function of both swelling and heterogeneity of void distribution. In a nutshell, quasi-embrittlement can be explained by a local deformation mode at the local scale referred to as void coalescence in the ductile fracture literature, that leads to strain localization in a band perpendicular to the tensile loading direction. Structural effects coming from the geometry of tensile specimens and / or swelling gradient are shown to lead to lower values of the critical swelling. The theoretical and numerical predictions are found to rationalize the experimental observations regarding the effects of test specimen geometry and the differences that may be observed between different materials for a given swelling level.

While the analysis presented allows to rationalize the experimental results, some perspectives could be considered. The assumption underlying Eq. 3 is that only irradiation-induced nanovoids contribute to the porosity of the material. Voids may also be nucleated from inclusions, which is the common scenario in ductile fracture, and the high number of precipitates usually observed in highly irradiated stainless steels makes this plausible. The qualitative effect of nucleation will be to increase the porosity, and thus to precipitate the occurrence of quasi-embrittlement. The difficulty in incorporating nucleation in the current modelling lies into the lack of reliable void nucleation criteria. Even for micrometric inclusions, void nucleation is treated using phenomenological criteria, either stress- or strain-controlled [45]. For nanometric inclusions, size effects could also be expected. Experimental assessment of void nucleation from nanoprecipitates, either from debonding or cracking, is required. A second perspective lies into the homogenized model for porous materials used in this study. As stated previously, this model is the simplest one incorporating both void growth and void coalescence regimes and based on a micromechanical approach. An assumption used is to consider spherical voids, which is relevant at the initial state. However, void shapes evolve under deformation, affecting ductility [44]. Refined homogenized models are available accounting for void shape that can be used in further studies. The effect on the critical swelling leading to embrittlement is however expected to be weak as embrittlement has been shown to come from a localization phenomenon occurring at low strains. Another assumption used is the isotropic behavior of the matrix surroundings voids, while nanovoids lies inside grains, thus in single crystals. Moreover, in the case of heterogeneous swelling, voids may be found predominantly at - or close to - grain boundaries. This leads to the question of the effect of the grain boundary of the path followed by a ductile crack.

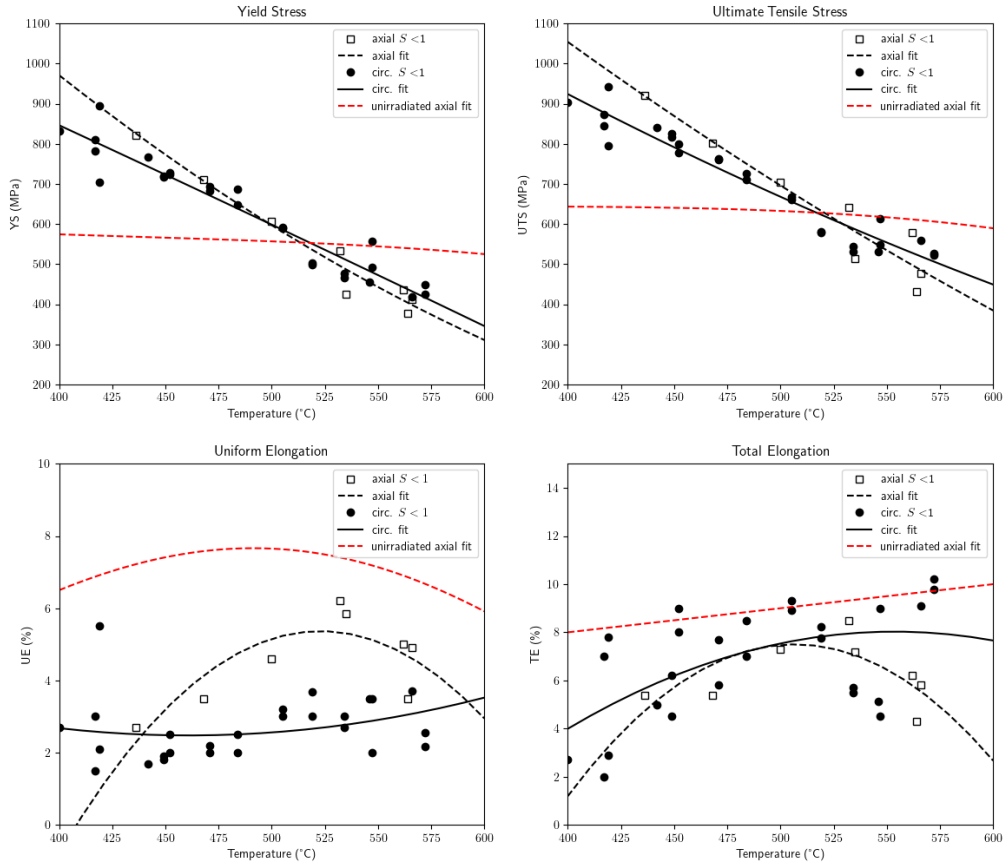
Acknowledgements

This paper is the result of a collaborative work involving many persons at the LECI hot laboratory. The authors wish to thank D. Schildknecht, M. Bonargent, R. Bouvy for manufacturing irradiated tensile specimens, P. Grange, J. Pegaitaz, T. Perez for performing recent tensile tests in hot cells and M. Sonnaert for density measurements. We gratefully thank B. Verhaeghe, C. Dessrouer, V. Cloute-Cazalaa for the preparation of TEM irradiated thin foils and S. Urvoy, C. Mallet, M. Azera for the SEM sample preparation and observation. Support from LECI hot cells staff is also greatly acknowledged.

CRedit authorship contribution statement

J. Hure: Conceptualization, Formal analysis, Methodology, Software, Writing - original draft **A. Courcelle:** Conceptualization, Investigation, Formal analysis, Writing - original draft **I. Turque:** Investigation, Writing - review & editing

Fig. 20 summarizes the evolution of conventional tensile properties of neutron-irradiated 15-15Ti as a function of temperature, for limited swelling $S < 1\%$. For a given specimen geometry, some variability is observed, especially for uniform and total elongations, that can be attributed to two causes. Slight differences in chemical composition shown and discussed along with Table 2 can explain part of the variations. For uniform and total elongations, reminding that both correspond to material instability (necking for the former, fracture for the latter), variations can be due to some imperfections of the specimen geometries. More precisely, for total elongation, the different shape of the cross section is known to affect ductility as leading to different stress states [53]. For the uniform elongation, a slight structural effect due to the bending of the gage length might play a role. However, clear trends can be observed, and trend curves have been calibrated and used to normalize the data (Eq. 2). For completeness, fitting curves of the experimental results for the unirradiated material are also given. The monotonic evolution of yield stress and ultimate tensile strength with temperature for both unirradiated and irradiated materials is rather classical. Non-monotonic evolutions of the elongations are observed, also reported for 316L austenitic stainless steel [54] and related to Dynamic Strain Ageing (DSA). As stated in [54], the link between DSA and ductility remains however to be clarified. At the unirradiated state, these curves are consistent with results obtained on a similar material in this temperature range [55].



(a)

Fig. 20. Comparison of axial and ring tensile tests (using test geometries shown on Fig. 2) at swelling lower than 1%. Solid and dashed lines correspond to calibration of the data by polynomial functions. Red curves are fits of unirradiated data (for axial specimen) on 15-15Ti.

Appendix B: Elastoplastic tangent matrix C

The bifurcation analysis presented in Section 3.2 requires the computation of the elastoplastic tangent matrix C defined as:

$$\dot{\sigma} = C : \dot{\varepsilon} \quad (13)$$

The generic expression for porous constitutive equations is given in [49]:

$$C = C^e - \frac{1-f}{h} (C^e : N) \otimes (C^e : N) \quad (14)$$

where C^e is the Hooke's elasticity fourth order tensor defined as $C_{ijkl}^e = \lambda \delta_{ij} \delta_{kl} + \mu (\delta_{ik} \delta_{jl} + \delta_{il} \delta_{jk})$, with λ and μ the Lamé

elastic parameters. N and h are the direction of plastic flow and a parameter defined as:

$$\begin{aligned} N &= \frac{\partial \sigma_{eq}}{\partial \sigma} \\ h &= (1-f)N : C^e : N + H - (1-f)^2 \frac{\partial \sigma_{eq}}{\partial f} N : \mathbf{1} \end{aligned} \quad (15)$$

For void growth equivalent stress (Eq. 5):

$$\begin{aligned} \frac{\partial \sigma_{eq}}{\partial \sigma} &= \frac{3s^* + q \sinh(1.5\sigma_m^*) \mathbf{1}}{2\sigma_{vM}^{*,2} + 3qf\sigma_m^* \sinh(1.5\sigma_m^*)} \\ \frac{\partial \sigma_{eq}}{\partial f} &= \frac{2q \sinh(1.5\sigma_m^*) - 2q^2 f}{2\sigma_{vM}^{*,2} + 3qf\sigma_m^* \sinh(1.5\sigma_m^*)} \end{aligned} \quad (16)$$

where $(\bullet)^* = \bullet / \sigma_{eq}$. For void coalescence equivalent stress (Eq. 6):

$$\begin{aligned} \frac{\partial \sigma_{eq}}{\partial \sigma} &= \left[(1-\chi^2) \left(0.1 \left(\frac{\chi^{-1}-1}{W} \right)^2 + 1.2 \sqrt{\chi^{-1}} \right) \right]^{-1} e_I \otimes e_I \\ \frac{\partial \sigma_{eq}}{\partial f} &= \frac{\partial \sigma_{eq}}{\partial \chi} \frac{\partial \chi}{\partial f} \\ \frac{\partial \sigma_{eq}}{\partial \chi} &= \frac{20W^2 \chi^{\frac{3}{2}} \left(\chi^{\frac{9}{2}} + 9W^2 \chi^4 - \chi^{\frac{7}{2}} + 3W^2 \chi^2 - \chi^{\frac{3}{2}} + \sqrt{\chi} \right)}{(\chi-1)^2 (\chi+1)^2 \left(\chi^{\frac{5}{2}} + 12W^2 \chi^2 - 2\chi^{\frac{3}{2}} + \sqrt{\chi} \right)^2} \sigma_I \\ \frac{\partial \chi}{\partial f} &= \frac{2\lambda}{\pi} \left(\frac{6f\lambda}{\pi} \right)^{-2/3} \end{aligned} \quad (17)$$

References

- 510 [1] G. Was, *Fundamentals of Radiation Materials Science: Metals and Alloys*, Springer, 2007.
- [2] S. Zinkle, P. Maziasz, R. Stoller, Dose dependence of the microstructural evolution in neutron-irradiated austenitic stainless steel, *J. Nuc. Mat.* 206 (1993) 266–286.
- [3] C. Cawthorne, E. Fulton, Voids in irradiated stainless steel, *Nature* 216 (1967) 575–576.
- [4] J. Straalsund, R. Powell, B. Chin, An overview of neutron irradiation effects in LMFBR materials, *J. Nuc. Mat.* 108-109 (1982) 299–305.
- 515 [5] S. Porollo, S. Shulepin, Y. Konobeev, F. Garner, Influence of silicon on swelling and microstructure in russian austenitic steel EI-847 irradiated to high neutron doses, *J. Nuc. Mat.* 378 (2008) 17–24.
- [6] F. Garner, Recent insights on the swelling and creep of irradiated austenitic alloys, *J. Nuc. Mat.* 122-123 (1984) 459–471.
- [7] P. Yvon, *Structural Materials for Generation IV Nuclear Reactors*, Elsevier, 2017, Ch. Irradiation-resistant austenitic stainless steels as core materials for Generation IV nuclear reactors, pp. 285–328.
- 520 [8] R. Konings, R. Stoller, *Comprehensive Nuclear Materials*, Elsevier, 2020, Ch. Radiation-induced Damage in Austenitic Structural Steels Used in Nuclear Reactors, pp. 57–168.
- [9] O. Chopra, A. Rao, A review of irradiation effects on LWR core internal materials: Neutron embrittlement, *J. Nuc. Mat.* 412 (2011) 195–208.
- [10] O. Chopra, A. Rao, A review of irradiation effects on LWR core internal materials: IASCC susceptibility and crack growth rates of austenitic stainless steels, *J. Nuc. Mat.* 409 (2011) 235–256.
- 525 [11] M. L. Hamilton, F.-H. Huang, W. J. Yang, F. A. Garner, Mechanical properties and fracture behavior of 20% cold-worked 316 stainless steel irradiated to very high neutron exposures, in: *Influence of Radiation on Material Properties: 13th International Symposium (Part II)*, ASTM International, 1987.
- [12] D. Porter, F. Garner, Irradiation creep and embrittlement behavior of AISI 316 stainless steel at very high neutron fluences, *J. Nuc. Mat.* 159 (1988) 114–124.
- 530 [13] S. Porollo, A. Vorobjev, Y. Konobeev, A. Dvoriashin, V. Krigan, N. Budylykin, E. Mironova, F. Garner, Swelling and void-induced embrittlement of austenitic stainless steel irradiated to 73-82 dpa at 335-365 degrees, *J. Nuc. Mat.* 258-263 (1998) 1613–1617.
- [14] V. Neustroev, F. Garner, Very high swelling and embrittlement observed in a Fe18Cr10NiTi hexagonal fuel wrapper irradiated in the BOR-60 fast reactor, *J. Nuc. Mat.* 378 (2008) 327–332.
- [15] V. Neustroev, F. Garner, Severe embrittlement of neutron irradiated austenitic steels arising from high void swelling, *J. Nuc. Mat.* 286-288 (2009) 157–160.
- 535 [16] A. Hojna, Overview of Intergranular Fracture of Neutron Irradiated Austenitic Stainless Steels, *Metals* 7 (2017) 392.
- [17] C. F. Tipper, The fracture of metals, *Metalurgia* 39 (1949) 133–137.
- [18] K. E. Puttick, Ductile fracture in metals, *Phil. Mag.* 4 (1959) 964–969.
- [19] A. S. Argon, J. Im, R. Safoglu, Cavity formation from inclusions in ductile fracture, *Metallurgical Transaction A* 6A (1975) 825–837.
- 540 [20] J. R. Rice, D. M. Tracey, On the ductile enlargement of voids in triaxial stress fields, *J. Mech. Phys. Sol.* 17 (1969) 201–217.
- [21] L. M. Brown, J. D. Embury, The initiation and growth of voids at second phase particles, Vol. 3rd International Conference on the strength of metals and alloys, 1973, pp. 164–168.
- [22] J. Koplik, A. Needleman, Void growth and coalescence in porous plastic solids, *Int. J. Sol. Struct.* 24 (1988) 835–853.
- 545 [23] A. Gurson, Continuum theory of ductile rupture by void nucleation and growth: Part I - Yield criteria and flow rules for porous ductile media, *J. Eng. Mat. and Tech.* 99 (1977) 2–15.
- [24] P. F. Thomason, A three-dimensional model for ductile fracture by the growth and coalescence of microvoids, *Acta Metall.* 33 (1985) 1087–1095.
- [25] A. Benzerga, J. Leblond, A. Needleman, V. Tvergaard, Ductile failure modeling, *Int. J. Frac.* 201 (2016) 29–80.
- [26] A. Pineau, A. Benzerga, T. Pardoen, Failure of metals I: Brittle and ductile fracture, *Acta Mat.* 107 (2016) 424–483.
- 550 [27] H. Chang, J. Segurado, O. R. de la Fuente, B. Pabón, J. LLorca, Molecular dynamics modeling and simulation of void growth in two dimensions, *Mod. Sim. Mat. Sci. Eng.* 21 (2013) 075010.
- [28] J. Hure, P. Barrioz, B. Tanguy, Assessing size effects on the deformation of nanovoids in metallic materials, *Scripta Mat.* 177 (2020) 54–57.
- [29] H. Yamamoto, Conditions for shear localization in the ductile fracture of void-containing materials, *Int. J. Frac.* 14 (1978) 347–365.
- [30] B. Margolin, A. Sorokin, V. Smirnov, V. Potapova, Physical and mechanical modelling of neutron irradiation effect on ductile fracture. Part 1. Prediction of fracture strain and fracture toughness of austenitic steels, *J. Nuc. Mat.* 452 (2014) 595–606.

- 555 [31] B. Margolin, A. Sorokin, Physical and mechanical modelling of neutron irradiation effect on ductile fracture. Part 2. Prediction of swelling effect on drastic decrease in strength, *J. Nuc. Mat.* 452 (2014) 607–613.
- [32] B. Margolin, A. Sorokin, V. Shvetsova, A. Minkin, V. Potapova, V. Smirnov, The radiation swelling effect on fracture properties and fracture mechanisms of irradiated austenitic steels. Part I. ductility and fracture toughness, *J. Nuc. Mat.* 480 (2016) 52–68.
- 560 [33] P. Vincent, H. Moulinec, L. Joëssel, M. Idiart, M. Garajeu, Porous polycrystal plasticity modeling of neutron-irradiated austenitic stainless steels, *J. Nuc. Mat.* 542 (2020) 152463.
- [34] A. Maillard, H. Tournon, J. Séran, A. Chalony, in: *Effects of Radiation on Materials: Sixteenth International Symposium, 1994*, pp. 824–837.
- [35] J. Séran, M. Le Flem, in: *Structural Materials for Generation IV Nuclear Reactors*, Woodhead Publishing, 2017, pp. 285–328.
- [36] M. Kirly, D. M. Antk, L. Horvth, Z. Hzer, Evaluation of axial and tangential ultimate tensile strength of zirconium cladding tubes, *Nuclear Engineering and Technology* 50 (3) (2018) 425–431.
- 565 [37] Y. Sekio, S. Yamashita, N. Sakaguchi, H. Takahashia, Void denuded zone formation for Fe15Cr15Ni steel and PNC316 stainless steel under neutron and electron irradiations, *J. Nuc. Mat.* 458 (2015) 355–360.
- [38] W. Liu, J. Yanzhou, T. Pengkang, Z. Hang, H. Chaohui, Y. Di, Z. Chi, Z. Y., Irradiation induced microstructure evolution in nanostructured materials: A review, *Materials* 9 (2016) 105.
- [39] P. Maziasz, Formation and stability of radiation-induced phases in neutron-irradiated austenitic and ferritic steels, *Journal of Nuclear Materials* 169 (1989) 95–115.
- 570 [40] S. Zinkle, P. Maziasz, R. Stoller, Dose dependence of the microstructural evolution in neutron-irradiated austenitic stainless steel, *Journal of Nuclear Materials* 206 (2) (1993) 266–286.
- [41] I. Balachov, E. Shcherbakov, A. Kozlov, I. Portnykh, F. Garner, Influence of radiation-induced voids and bubbles on physical properties of austenitic structural alloys, *J. Nuc. Mat.* 329-333 (2004) 617–620.
- 575 [42] V. Tvergaard, On localization in ductile materials containing spherical voids, *Int. J. Frac.* 18 (1980) 237–252.
- [43] V. Tvergaard, A. Needleman, Analysis of the cup-cone fracture in a round tensile bar, *Acta Metall.* 52 (1984) 157–169.
- [44] A. A. Benzerga, J.-B. Leblond, Ductile fracture by void growth to coalescence, *Adv. Applied Mech.* 44 (2010) 169–305.
- [45] J. Besson, Continuum models of ductile fracture: a review, *Int. J. Dam. Mech.* 19 (2010) 3–52.
- [46] J. Scherer, J. Hure, A size-dependent ductile fracture model: Constitutive equations, numerical implementation and validation, *Eur. J. Mech. A/Solids* 76 (2019) 135–145.
- 580 [47] T. Helfer, B. Michel, J. Proix, M. Salvo, J. Sercombe, M. Casella, Introducing the open-source mfront code generator: Application to mechanical behaviours and material knowledge management within the pleiades fuel element modelling platform, *Computers & Mathematics with Applications* 70 (2015) 994–1023.
- [48] M. Shokeir, J. Hure, T. Helfer, Extension of the standardelastoviscoplasticity brick to porous materials, https://www.researchgate.net/publication/346484549_Extension_of_the_StandardElastoViscoPlasticity_brick_to_porous_materials.
- 585 [49] J. Besson, D. Steglich, W. Brcks, Modeling of crack growth in round bars and plane strain specimens, *Int. J. Sol. Struct.* 38 (2001) 8259–8284.
- [50] J. Rice, The localization of plastic deformation, Vol. 14th International Congress on Theoretical and Applied Mechanics, 1976, pp. 207–220.
- [51] CEA, Cast3m, www-cast3M.cea.fr.
- [52] M. Considère, Mémoire sur l’emploi du fer et de l’acier dans les constructions, *Annales des Ponts et Chaussées IX* (1885) 574–775.
- 590 [53] I. Khan, A. Srivastava, A. Needleman, A. Benzerga, An analysis of deformation and failure in rectangular tensile bars accounting for void shape changes, *International Journal of Fracture* 230.
- [54] G. Meric de Bellefon, J. van Duysen, Tailoring plasticity of austenitic stainless steels for nuclear applications: Review of mechanisms controlling plasticity of austenitic steels below 400°C, *Journal of Nuclear Materials* 475 (2016) 168–191.
- 595 [55] E. Curtet, B. Kedjar, F. Momprou, H. Bahsoun, F. Pailloux, A. Courcelle, M. Bono, P. Olier, L. Thilly, Loss of ductility in optimized austenitic steel at moderate temperature: A multi-scale study of deformation mechanisms, *Materialia* 9 (2020) 100562.